Deformation mechanisms in the α phase of the Ti-6Al-2Sn-4Zr-2Mo titanium alloy: In situ experiments and simulations

S. Hémery, A. Naït-Ali, O. Smerdova, Christophe Tromas

To cite this version:

S. Hémery, A. Naït-Ali, O. Smerdova, Christophe Tromas. Deformation mechanisms in the α phase of the Ti-6Al-2Sn-4Zr-2Mo titanium alloy: In situ experiments and simulations. International Journal of Plasticity, 2024, 175, pp.103947. ⟨10.1016/j.ijplas.2024.103947⟩. ⟨hal-04569970⟩

International Journal of Plasticity 175 (2024) 103947

Contents lists available at ScienceDirect

International Journal of Plasticity

journal homepage: www.elsevier.com/locate/ijplas

Deformation mechanisms in the α phase of the Ti-6Al-2Sn-4Zr-2Mo titanium alloy: In situ experiments and simulations

S. Hémery [*], A. Naït-Ali, O. Smerdova, C. Tromas

Institut Pprime, ISAE-ENSMA, Université de Poitiers, CNRS UPR 3346, Téléport 2, 1 avenue Clément Ader, BP 40109, Futuroscope-Chasseneuil Cedex 86961, France

ARTICLE INFO

Keywords:
Titanium
Anisotropic material
Microstructures
Crystal plasticity
Mechanical testing

ABSTRACT

Titanium alloys are widely employed in aerospace applications due to an outstanding combination of properties. The variety of loading conditions and microstructures encountered in industrial components is urging the development of microstructure sensitive modeling capabilities. In particular, reliable predictions require a good knowledge of operating deformation mechanisms. The present study aims at providing a thorough characterization of deformation mechanisms in the near-α Ti-6Al-2Sn-4Zr-2Mo alloy using experiments and simulations. The sequential activation of deformation mechanisms in the α phase was monitored in situ during a tensile test carried out in a scanning electron microscope using a combination of slip traces analysis and electron back-scattered diffraction. Basal slip is activated first, and prismatic slip activity, which proceeds at a higher macroscopic stress level, is needed for a significant creep/relaxation to occur. While little evidence of $\langle a \rangle$-type pyramidal slip was found, $\langle c + a \rangle$ pyramidal slip involved first-order pyramidal planes and operates at stress levels near or above the 0.2% proof stress. Atomic force microscopy characterization of the features of the different slip modes revealed that $\langle a \rangle$ slip is coarser and wavier than $\langle c + a \rangle$ slip. Twinning, which is usually neglected in such alloys within this strain regime, was observed to be slip stimulated at a plastic strain as low as 0.5%. Crystal plasticity parameters leading to an accurate simulation of the activation sequence of deformation mechanisms were then determined. For this purpose, critical resolved shear stress values were derived for the different slip and twinning modes using specific approaches and subsequently validated using crystal plasticity simulations based on fast-Fourier transforms.

1. Introduction

Near-α titanium alloys, such as Ti-6Al-2Sn-4Zr-2Mo, are extensively used for high temperature applications in gas turbine engines in the aerospace industry due to superior properties including a high creep resistance (Gerd Lütjering, James C. Williams, 2007). Tailoring of microstructure and composition is currently a topic of intense research in order to reach higher operation temperatures. Over the past decades, crystal plasticity finite elements models became a key tool for an improved understanding of the interplay between microstructure and deformation in Ti alloys (Lhadi et al., 2018; Smith et al., 2018a; Venkatramani et al., 2007; Waheed et al., 2019). Specific features of titanium alloys have been incorporated in the simulations such as microstructural arrangements resulting

---

[*] Corresponding author.
E-mail address: samuel.hemery@ensma.fr (S. Hémery).

https://doi.org/10.1016/j.ijplas.2024.103947
Received 12 January 2024; Received in revised form 14 March 2024;
Available online 15 March 2024

from Burgers orientation relationships (Deka et al., 2006; Venkatramani et al., 2007; Waheed et al., 2019; Zheng et al., 2018), and room temperature creep deformation (Dunne et al., 2007a; Hasija et al., 2003a; Neeraj et al., 2000). These developments have led to an improved mechanistic understanding of dwell fatigue lifetime debits due the load hold periods at peak stress through simulations of the deformation behavior in microstructural configurations associated with crack initiation (Dunne et al., 2007b; Hasija et al., 2003a; Shen et al., 2022). The consequences of microtextured regions arising from the applied thermo-mechanical processing route (Semiatin, 2020) are also being addressed owing to increasing computational capabilities and novel simulation techniques (Cappola et al., 2020; Hémery et al., 2019; Liu and Dunne, 2020; Nait-Ali et al., 2021). For instance, crystal plasticity simulations based on fast-Fourier transforms allowed to consider realistic microstructural regions at the millimeter scale and unravel the consequences of the presence of microtextured regions on the mechanical response (Hémery et al., 2019). In spite of advanced models incorporating complex interactions between microstructure and deformation, a recent study highlighted the critical need for experimental inputs to obtain an accurate simulation of the experimental behavior (Tari et al., 2018).

Microplasticity at room temperature in Ti alloys was recently reviewed (Hémery et al., 2020). As the hexagonal closed-packed (HCP) α phase accounts for more than 90% of the surface fraction and governs the deformation and fatigue damage of near-α and α+β alloys, this phase has been the subject of continuous research efforts (Pagan et al., 2023). It is well established that basal and prismatic slip system are the main deformation systems operating in Ti – 6 wt.% Al based alloys (Bridier et al., 2005; Echlin et al., 2016; Hémery et al., 2018a; Hémery and Villechaise, 2017a). Although prior studies showed that they exhibit quite similar critical resolved shear stress (CRSS) values, in situ SEM monitoring of slip activation has demonstrated that basal slip is activated first (Dichtl et al., 2022; Echlin et al., 2016; Hémery et al., 2018a; Hémery and Villechaise, 2017a). This feature is believed to stem from the elastic anisotropy of HCP α phase: α grains well oriented for basal slip generally experience higher stress than α grains well oriented for prismatic slip (Hémery et al., 2019; Hémery et al., 2018b). However, this critical feature is generally not validated for CRSS datasets reported in the literature. Also, α grains deforming via basal slip experience higher strains (Charpagne et al., 2020; Hémery and Villechaise, 2019) and exhibit higher strain rate sensitivities (Zhang et al., 2016a, 2016b) than α grains deforming via prismatic slip. Pyramidal slip activity involving an $<a>$-type Burgers vector is less documented. While some observations were reported (Zaefferer, 2003), slip traces analysis involving statically meaningful numbers of observations showed that $<a>$-type pyramidal slip is rare (Bridier et al., 2005; Hémery and Villechaise, 2017a). Notably, cross-slip of $\langle \mathrm{a} \rangle$ dislocations onto pyramidal planes was suggested (Castany et al., 2007).

$<a>$-type slip cannot accommodate the c-axis deformation of the HCP lattice, which relies on the operation of $<c+a>$-type slip or twinning. The former is generally observed to be active in Ti alloys containing 6 wt.% Al (Zaefferer, 2003). Unless TEM analysis or advanced digital image correlation techniques involving Burgers vector identification are used, slip traces analysis leads to a difficult discrimination of $\langle \mathrm{a} \rangle$ and $\langle c+a \rangle$ slip as both can proceed on first-order pyramidal planes. As a consequence, statistical data about $\langle c+a \rangle$ slip in polycrystalline materials has not been reported to the best of the authors' knowledge. The reported tension – compression anisotropy (Jones and Hutchinson, 1981a; Roberts et al., 2020) and the possible glide along first- and second- order pyramidal planes further complicates the analysis (Gerd Lütjering, James C. Williams, 2007). This results in (i) a high scatter in the reported CRSS values, (ii) an unclear crystallographic orientation domain where it is likely to operate and, in turn, (iii) an imprecise assessment of its contribution to the deformation. Finally, twinning is generally held inactive in Ti alloys with a high Al content due to the inhibiting effect of short range order (Fitzner et al., 2016). However, many recent studies have shown that twinning can operate at moderate strains although the lower bound of the strain range is not clear yet (Lavogiez et al., 2018; Prakash et al., 2010). While a minor contribution to the macroscopic deformation behavior is expected, an important role could be played under cyclic loadings (Lavogiez et al., 2018; Ma et al., 2017).

As suggested in the previous paragraphs, deformation of Ti alloys in the strain regime relevant for cyclic loadings such as experienced in service still deserve complementary characterization. For instance, an accurate description of the sequential activation of the various deformation systems is still missing from literature data, though critical for a physically realistic simulation of the deformation behavior. In addition, CRSS datasets available in the literature, which sometimes do not include pyramidal slip systems or twinning, generally lack validation against grain scale experimental data to demonstrate the degree of reliability of the reported values. Another important question pertains to the relation between creep deformation, which is key in the reduction in cycles to failure occurring under dwell-fatigue loading for example (Liu et al., 2021; Venkatramani et al., 2007), and the operating deformation mechanisms. Individual behaviors of basal and prismatic slip systems (Chatterjee et al., 2017; Zhang et al., 2016a, 2016b), or the macroscopic viscoplastic response (Imam and Gilmore, 1979; Kapoor et al., 2020; Khan et al., 2004; Neeraj et al., 2000; Ruiz de Sotto et al., 2020) have been characterized. However, no clear relationship between the sequential activation of deformation mechanisms and the viscoplastic response of the material has been reported to the best of the authors' knowledge. Finally, the character of the different slip modes, including an assessment of slip waviness, bands spacing and localization, is of fundamental importance to understand the deformation behavior (Brandes et al., 2010; Welsch and Bunk, 1982) and the fatigue performance (Risbet et al., 2003; Stinville et al., 2022). In addition to a decades long interest (Margolin and Longo, 1979; Truax and McMahon, 1974; Williams et al., 1974), this topic has recently received an increasing attention with the development of high-resolution digital image correlation (Charpagne et al., 2020; Dhekne et al., 2023; Hu et al., 2023; Lagattu et al., 2006; Lunt et al., 2017). This technique provides an unmatched capability to study large regions, but can be limited by its spatial resolution and hypothesis used in continuum mechanics (Bourdin et al., 2018). Complementary analyses using atomic force microscopy, which can overcome these limitations over a more restricted area of interest, have not been reported yet to the best of the authors' knowledge. The motivations of the presently reported work are based on these knowledge gaps.

In this study, an in-situ scanning electron microscope (SEM) tensile test was carried out on a Ti-6Al-2Sn-4Zr-2Mo specimen. In situ tensile testing in a SEM is a key tool to monitor the activation of deformation mechanisms as a function of the applied loading while maintaining a statistically significant number of observations (Barkia et al., 2015; Hémery and Villechaise, 2017a; Li et al., 2015; Wei et al., 2022). While this technique can present disadvantages as compared to X-ray diffraction based approaches that provide a straightforward assessment of lattice strains in the bulk (Chakraborty et al., 2020; Miller et al., 2020), active deformation mechanisms such as slip modes can be directly identified. However, a restricted amount of studies have aimed at using the associated data in order to extract CRSS datasets with a dedicated approach (Hémery et al., 2017a; Li et al., 2013). For the sake of simplicity, deformation was studied in equiaxed α grains to address the important knowledge gaps highlighted previously. Slip traces analysis and EBSD characterization were employed to identify active deformation mechanisms as a function of the macroscopic stress / strain state while considering a statistically significant number of grains. Threshold macroscopic stress or strain states to activate the different deformation modes were then determined and correlated with the stress relaxation or creep kinetics. Characterization of the slip features was also performed using atomic force microscopy (AFM), which complemented SEM based techniques through offering access to quantitative nanoscale information. Critical resolved shear stress (CRSS) values were then derived from the collected data using specific methodologies, including a Eshelby-Kröner self-consistent approach accounting for free surface effects, and validated at the α grain scale against fast-Fourier transforms based full-field crystal plasticity (CP) simulations. This methodology ensured to provide a set of parameters allowing an accurate simulation of active slip modes in future crystal plasticity studies.

2. Material and experiments

2.1. Material

Ti-6Al-2Sn-4Zr-2Mo (Ti-6242) provided by Timet was used in the present study. The measured composition given by the manufacturer is Ti-6.08Al-1.96Mo-3.90Zr-1.97Sn-0.11O-0.07Si in weight percent. Internal stress resulting from billet processing in the α+β field were relieved using an annealing treatment for several hours at 750 °C. A final aging treatment of 8 h at 595 °C was applied in order to promote α_2 precipitation. The resulting microstructure is shown in Fig. 1a. The average diameter of primary α grains is about 10 µm. They account for 65% of the area fraction. Transformed beta regions containing a bi-modal distribution of α plates embedded in residual β phase account for the remaining 35%. The thickness of secondary α plates is approximately 1 µm. This value was obtained using more than 100 manual measurements carried out on SEM micrographs. Tertiary α plates with a thickness in the 50 nm range are present within residual β layers. An inverse pole figure map showing the local crystallographic orientations is presented in Fig. 1b and reveals the presence of microtextured regions with a characteristic size of a few hundreds of micrometers. The orientation density function of the α phase is plotted on an inverse pole figure (IPF) in Fig. 1c. Only points with a confidence index higher than 0.1 were considered for the texture calculation. The maximum intensity is lower than 2 times random. This value indicates a weak texture which

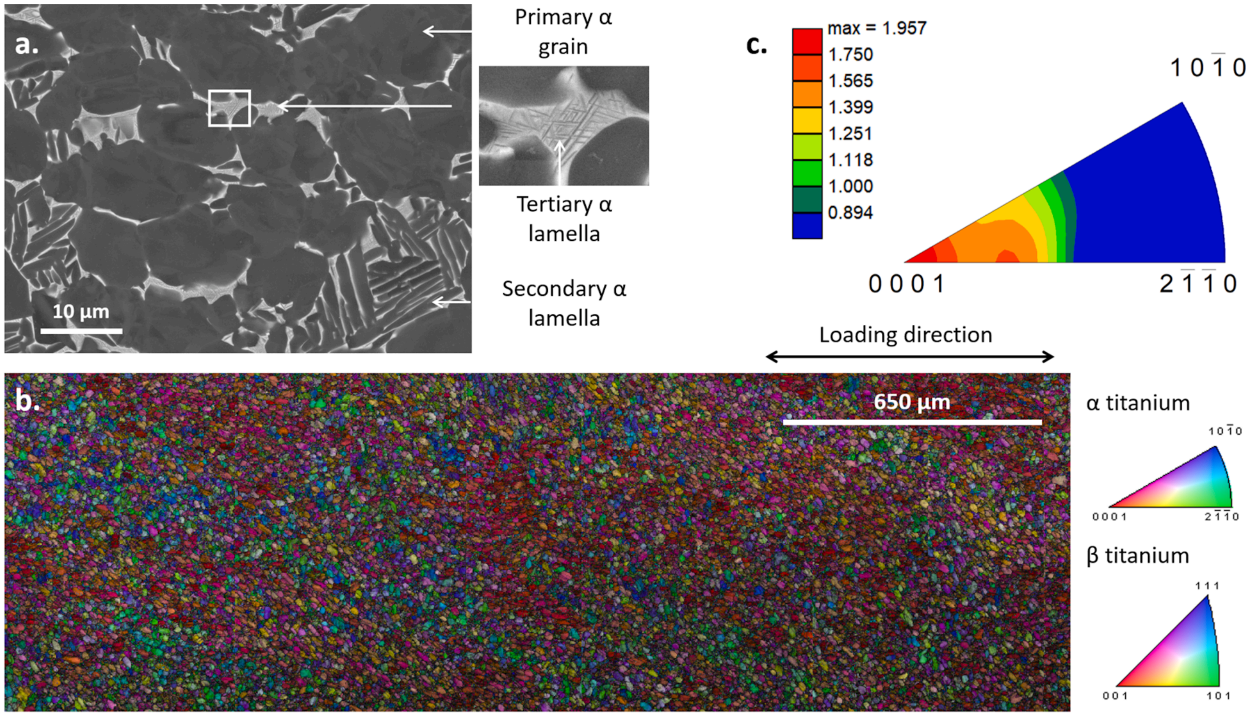

Fig. 1. a. SEM micrograph showing the microstructure of the Ti-6242 alloy employed in the present study, b. Inverse pole figure superimposed with the image quality map showing crystallographic orientations relative to the loading direction and the degree of microtexture, and c. Orientation density function relative to the loading direction plotted on an inverse pole figure.

corresponds to a preferential alignment of the [0001] direction with the loading axis. Tensile properties were assessed using strain rates of $10^{-4}\ s^{-1}$ and $10^{-2}\ s^{-1}$. Nominal stress – strain curves are reported in Fig. 2a. The yield strengths calculated using a 0.2% plastic strain offset are 916 MPa and 966 MPa respectively. The ultimate tensile strengths are 984 MPa and 1013 MPa. Elongations at failure are 15.5% and 13.7%. The Young's modulus is about 120 GPa.

2.2. *In situ SEM tensile test*

A dogbone shaped tensile specimen was machined using electrical discharge machining. The gage length was 10 mm and the gage width was 2 mm. Both faces were ground using SiC paper up to 4000 grade. Finally, one face was polished using a diamond suspension with 9 μm particles before finishing with a mixture of a colloidal solution containing 0.04 μm silica particles and 10% hydrogen peroxide. The resulting thickness of the specimen was about 800 μm. The specimen was tested in tension in a JEOL 6100 SEM using a Deben tensile stage equipped with a 5 kN loadcell. A 0.02 mm min^{-1} displacement rate, which is roughly equivalent to $3 \times 10^{-5}\ s^{-1}$, was applied during loading. In order to monitor operating deformation mechanisms, the displacement was stopped at targeted macroscopic stress values and several regions of interest were observed. The strain was estimated at each stop using metallurgical markers. All stress and strain values reported throughout the article are nominal. The first stop was achieved at a load corresponding to 500 MPa. To maintain an accurate description of the activation of deformation mechanisms during loading, the macroscopic stress increments were progressively decreased. 50 MPa increments were applied up to 600 MPa. 20 MPa steps were then applied and 10 MPa steps were used from 650 MPa to 840 MPa. The resulting nominal stress – strain curve is shown in Fig. 2. The 0.2% plastic strain offset was reached at the 810 MPa step. The low yield strength as compared to conventional tensile tests is expected to pertain mostly to the rate dependent mechanical behavior of titanium alloys at room temperature (Neeraj et al., 2000). The test was stopped at a load equivalent to 840 MPa which corresponds to 0.7% plastic strain.

As crosshead displacement control was used, stress relaxation and creep deformation occurred during the displacement hold. The evolution of the load as a function of the hold time is illustrated in Fig. 3a. The decrease in macroscopic stress after a 12 min displacement hold (Δσ) was used as a metric for stress relaxation / creep kinetics. While it does not provide a quantitative assessment of the strain rate sensitivity or creep exponent, insights into the relation between relaxation or creep behaviors and the macroscopic loading were extracted. Δσ values collected in the 650 MPa – 840 MPa range are plotted in Fig. 3b. This range was considered as similar macroscopic stress increments were applied. Near 650 MPa, the stress decreased by roughly 1 MPa in 12 min. As shown by the linear regressions plotted in Fig. 3b, this value is weakly increasing up to 780 MPa. A 5 MPa drop was noticed at this step. Beyond, the increasing rate of the stress drop as a function of the macroscopic stress was significantly higher. This reveals a transition in stress relaxation / creep kinetics near 780 MPa.

2.3. *Analysis of deformation mechanisms*

Slip traces analysis was carried out to identify active slip systems. Back-scattered electron micrographs were used for this purpose. In addition to topography information, the crystallographic orientation sensitivity was helpful to detect possible twinning. 3 regions of interest were followed during the whole test. Each region of interest was approximately 160 μm by 128 μm. An example is shown in Fig. 4a. Beyond 800 MPa, 4 additional regions of interest have been followed in order to study less frequently activated deformation systems with a statistical significance. Crystallographic orientations were obtained using the EBSD technique. A JEOL 6100 SEM equipped with a Hikari EBSD detector provided by EDAX was used for this purpose. A step size of 0.3 μm was applied. Crystallographic orientations along the loading direction in a region of interest are shown in Fig. 4a. Basal, prismatic and pyramidal plane traces were then calculated using an in-house program and compared to experimentally observed slip traces. This procedure is schematically shown in Fig. 4b for a slip trace appearing at the 660 MPa step. If multiple slip planes correspond to the experimentally observed plane

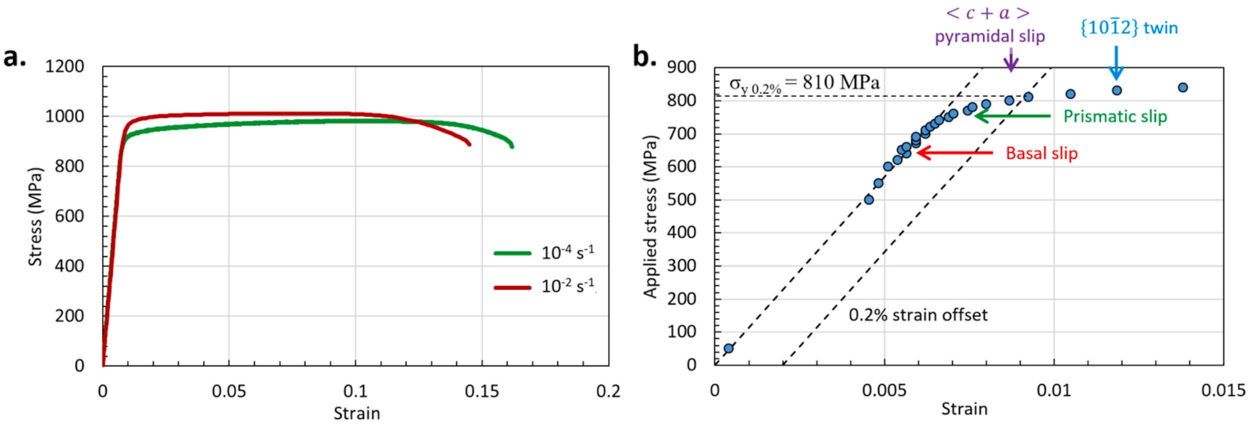

Fig. 2. a. Nominal stress – strain curves obtained using different strain rates, and b. Reconstructed engineering stress – strain curve of the tensile test carried out in situ in the SEM. The loading steps associated with the first observation of identified deformation mechanisms are indicated.

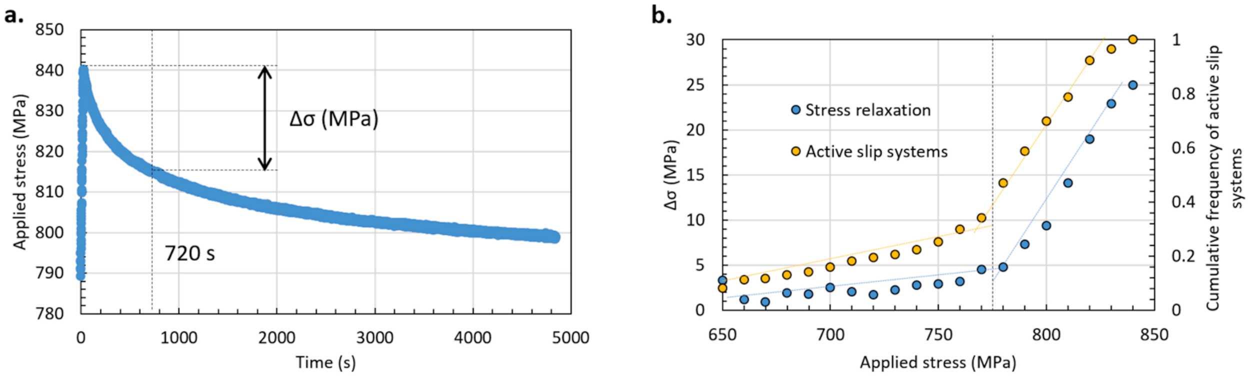

Fig. 3. a. Macroscopic stress evolution during a loading step followed by a displacement hold showing a load decrease resulting from the occurrence of stress relaxation and creep, and b. The decrease in stress after a 12 min displacement hold (Δσ) plotted with respect to the macroscopic stress. Linear regressions shown using dashed lines indicate the different regimes. The cumulative frequency of active slip systems in the region of interest is also presented. The stress relaxation behavior appears correlated with the number of active slip systems.

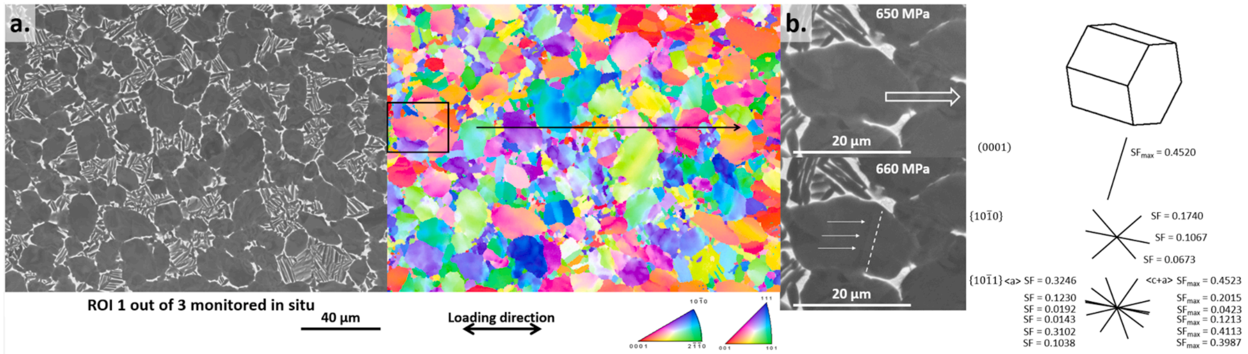

Fig. 4. a. Back-scattered electron micrograph and inverse pole figure map showing the microstructure and local crystallographic orientations with respect to the loading direction in a region of interest, and b. Example of a slip trace appearing at the 660 MPa step that corresponds to basal slip with a maximum Schmid factor of 0.4520.

trace within a ± 5° interval, this slip event is dismissed because its identification is ambiguous. It is dismissed as well if no plane trace matches the experimental trace within a ± 5° interval. Based on plane trace analysis, the active slip system is unambiguously identified for prismatic and ⟨a⟩ type pyramidal slip as only one slip direction matches each slip plane. However, several slip directions are associated with a slip plane for basal and $\langle c + a \rangle$ pyramidal slip. In that case, the slip system with the highest Schmid factor (*SF*) was assumed to be active. Prior studies have shown that Schmid's law with a global stress state approximation leads to a good agreement with experimental observations (Hémery and Villechaise, 2019; Xu et al., 2019).

Features of slip events were studied quantitatively using AFM after the final loading step. An Icon Dimension XR microscope manufactured by Brucker was used in peak force mode for this purpose. The slip step height and the slip trace spacing were assessed using topography data. A plane fitting correction was applied using flat terraces in between slip traces, before using a peak detection routine. Based on this information, slip distribution was qualified as "coarse" or "fine". The waviness of slip traces was also qualitatively evaluated to discuss slip planarity and the propensity to cross-slip. These terms were more thoroughly defined in a previous study (Williams et al., 1974). Three occurrences were considered for each slip mode to ensure a good representativity of similarities and differences in slip character.

Twin formation during tensile testing was primarily monitored using in situ SEM observations. The twinning system was determined after unloading at the end of the test. A JEOL 7000F field emission gun SEM equipped with a DigiView EBSD detector provided by EDAX was used for this purpose. A 20 nm step size was applied. It is worth noting that SEM parameters such as the operation voltage and the probe size were adjusted to allow EBSD analysis with a high spatial resolution, which is needed due to the sub micrometric size of twins.

2.4. Critical resolved shear stress estimation

Accurate determination of CRSS values for deformation modes operating in Ti alloys is key for realistic crystal plasticity simulations and a proper reproduction of experimentally observed behaviors. Different approaches were applied in this study to derive CRSS from slip traces analysis. An elastic self-consistent approach was employed for slip modes operating at macroscopic stress lower than the yield stress. In this regime, slip activity is not homogeneously distributed and a significant fraction of the grains behaves elastically. In contrast with full-field simulations, the stress state of a particle embedded in a homogeneous medium is estimated. This feature is thus useful in order to dismiss stress heterogeneities resulting from a given grain neighborhood (Abdolvand et al., 2018; Bretin et al., 2019; Kawano et al., 2020). The CRSS values for the ss slip system (τ_c^{ss}) were calculated as follows:

$$\tau_c^{ss} = |\sigma : m^{ss}| \tag{1}$$

With m^{ss} the symmetric Schmid tensor for ss slip system and σ the grain averaged stress tensor determined using the self-consistent model described in Section 3.2. Each grain was considered as a spherical inclusion in a homogeneous effective medium. Simulations included approximately 2000 α grains with orientations sampled from the EBSD data presented in Fig. 1b, in addition to the orientation of α grains monitored in situ. This allowed to account for the texture of the specimen tested in situ. σ was determined at the macroscopic stress level associated with slip activation in the considered α grain. The following elastic constants, which correspond to the transversely isotropic α phase, were employed: C_{11}=162.4 GPa, C_{12}=92.0 GPa, C_{13}=69.0 GPa, C_{33}=180.7 GPa and C_{44}=46.7 GPa (Fisher and Renken, 1964). As the amount of retained β phase is low in Ti-6242, primary α grains and transformed β regions were not distinguished.

A different method was applied for deformation systems activated at a macroscopic stress higher than the yield strength since the behavior of the homogeneous medium cannot be approximated as elastic in this regime. The employed approach uses the competition between different deformation mechanisms in order to determine a CRSS ratio (Zaefferer, 2003). This has been successfully applied in prior studies (Barkia et al., 2015; Li et al., 2013). Li et al. proposed a specific procedure to obtain CRSS values based on slip traces analysis at a single deformation step (Li et al., 2013). Another example of such method applied to bound CRSS values is shown in the work of Barkia et al. (Barkia et al., 2015). Considering a uniaxial stress state in a grain where the *i* and *j* slip modes are competing, activity of the *i* slip system only reveals that the $\frac{\tau_c^i}{\tau_c^j}$ CRSS ratio must be higher than $\frac{SF^i}{SF^j}$. Statistical data is used to estimate the CRSS ratio leading to equal activation probability for *i* and *j* slip modes.

Differences in strength for primary α grains and transformed β regions were assessed using nano-indentation experiments. A Micromaterials NanoTest Vantage nano-indenter was employed in load control mode. A grid of 500 indents was performed with a Berkovich diamond tip using a peak load of 10 mN. The size of the indents was typically 2 to 3 μm and the spacing was set to 10 μm. The values of hardness were obtained from nanoindentation force-displacement curves using the Oliver and Pharr method (Oliver and Pharr, 1992).

3. Simulations techniques

Determination of the CRSS dataset and its validation involved different simulation techniques. Mean field models are efficient methods to simulate the average behavior of a statistically significant number of grains or the macroscopic response. In contrast, full field simulations such as finite elements or fast Fourier transforms based CP (CP-FFT) account for specific neighboring grain configuration including elastic and plastic interactions (Esqué-de los Ojos et al., 2018). Therefore, they provide a more accurate distribution of the behavior of individual grains, which was used for CRSS dataset validation. Details of the employed models are described in the following paragraphs.

3.1. *Fast-Fourier transforms based crystal plasticity modeling*

The model proposed by Lebensohn et al. (Lebensohn et al., 2012) was implemented in our FoXTRoT in-house simulation code. It was successfully employed to simulate the behavior of Ti alloys in prior studies (Ahmadikia et al., 2021; Bhattacharyya et al., 2021; Hémery et al., 2019; Nait-Ali et al., 2021). The elasto-viscoplastic formulation is briefly detailed in the following (Eqs. (2) and (3)) (Lebensohn et al., 2012). The plastic shear rate is computed using the following equation:

$$\dot{\gamma}^{ss}(x) = \dot{\gamma}_0 \left(\frac{|m^{ss}(x) : \sigma(x)|}{\tau_0^{ss}}\right)^{n-1} \times \left(\frac{m^{ss}(x) : \sigma(x)}{\tau_0^{ss}}\right) \tag{2}$$

Where $m^{ss}(.)$ is the Schmid tensor and $\dot{\gamma}^{ss}(.)$ is the shear strain rate on the *ss* slip system. In the following, $\varepsilon(.)$ and $\sigma(.)$ are the local values of strain and stress fields respectively. The viscoplastic strain velocity $\dot{\varepsilon}^{P}(.)$ is constitutively bound to the stress $\sigma(.)$ at a point of the monocrystalline material x by the following formula considering the N active slip systems:

$$\dot{\varepsilon}^{P}(x) = \sum_{ss=1}^{N} m^{ss}(x)\, \dot{\gamma}^{ss}(x) \tag{3}$$

By E, we denote the macroscopic strain tensor and by $C(.)$ the stiffness tensor that depends on the position vector x. The iterative FFT-algorithm used was originally proposed by Moulinec and Suquet (Moulinec and Suquet, 1998). It consists in polarizing the domain by introducing the reference support of stiffness and compliance, respectively. The algorithm is the following (Hémery et al., 2019):

$$\left\{\begin{array}{c} Initialisation: \\ \varepsilon^{0} = E \\ \sigma^{0}(x) = C(x) : \varepsilon^{0} \\ \\ Iterate\ k+1: \\ \sigma^{k},\ \ \varepsilon^{k} and\ \ \varepsilon^{p,k}\ are\ done \\ \widehat{\varepsilon}^{k}(\widehat{\xi}) = FFT\left(\varepsilon^{k}(x)\right) \\ \widehat{\varepsilon}^{k+1}(\widehat{\xi}) = -\widehat{\Gamma}_{0} : \widehat{\sigma}^{k}(\widehat{\xi}) + \widehat{\varepsilon}^{k}(\widehat{\xi}),\ if\ \widehat{\xi} \neq 0 \\ \widehat{\varepsilon}^{k+1}(\widehat{\xi}) = E,\ if\ \widehat{\xi} = 0 \\ \\ Mechanical\ field\ updates \\ \varepsilon^{k+1}\ (x) = FFT^{-1}\left(\widehat{\varepsilon}^{k+1}(\widehat{\xi})\right) \\ \sigma^{k+1}(x) = C(x) : \left(\varepsilon^{k+1}(x) - \ \varepsilon^{p,k}\ - \ \dot{\varepsilon}^{\,p,k+1}(x)\Delta t\right)\ \varepsilon^{p,k}\ =\ \varepsilon^{p,k}\ +\ \dot{\varepsilon}^{\,p,k+1}(x)\Delta t Convergence\ test \end{array}\right. \tag{4}$$

Where the symbol "^" indicates Fourier transform and $\widehat{\xi}$ is a frequency of Fourier space. The Green function $\widehat{\Gamma}_0$ was proposed in a previous study (Moulinec and Suquet, 1998). The algorithm requires a convergence test to stop the iterating process. This test consists in checking the equilibrium with a strain-controlled method. The criterion for the convergence in Real space is done classically (Moulinec and Suquet, 1998):

$$\| \varepsilon^{i+1} - \varepsilon^{i} \|_2 < 10^{-3} \left| \varepsilon^{0} \right| \tag{5}$$

where $\| \ . \ \|_2$ denotes the L2 norm and $|.|$ the Euclidian norm of second-order tensor. The applied step time guarantees a convergence of the solution for each increment. The algorithm was implemented in our FoXTRoT in-house simulation code using multithreading through the use of OpenMP directives and relies on libraries for matrix calculations (Eigen) and discrete Fourier transforms (FFTW library).

3.2. Self-consistent Eshelby-Kröner modeling

The classical Eshelby-Kröner model was employed in this study (Eshelby, 1957; Kröner, 1958). The equations are recalled in Eqs. (6) and (7). The crystallographic orientation in each α grain or transformed β region is considered using Euler angles. The homogenized stiffness C^{homo} is calculated iteratively through an averaging procedure on each crystallite as shown below:

$$C^{homo} = < C_i : \left[E_i : (C_i - C^{macro}) + I_4\right]^{-1} > \tag{6}$$

Here, C_i represents the elastic stiffness of grain i, and I_4 is the 4th-order Identity tensor. The Morris tensor, denoted as E_i, can be expressed in terms of the Eshelby tensor $\boldsymbol{S}_{Esh}$ using the relation (Morris, 1970):

$$E_i = \boldsymbol{S}_{Esh} C^{macro-1} \tag{7}$$

The calculation of the Morris tensor was carried out using numerical integration. The employed scheme is recalled in Eqs. (8) and (9) (Riyad et al., 2021). As an elasto- viscoplastic framework was considered, the evolution of the plastic strain for each individual grain was computed as follows:

$$\varepsilon_i^{p,k+1} \ = \ \varepsilon_i^{p,k} \ + \ \Delta\varepsilon_i^{p} \tag{8}$$

where $\varepsilon_i^{p,k}$ is the plastic strain at the current time step k, $\varepsilon_i^{p,k+1}$ is the plastic strain at the next time step, and $\Delta\varepsilon_i^{p}$ is the increment in plastic strain. The increment in plastic strain, $\Delta\varepsilon_i^{p}$, is given by:

$$\Delta\varepsilon_i^{p} = \sum_{ss=1}^{N} m_i^{ss} \dot{\gamma}_i^{ss} \Delta t \tag{9}$$

where m_i^{ss} is the Schmid tensor for the ss slip system in grain i, Δt is the time step and $\dot{\gamma}_i^{ss}$ is the shear strain rate of the ss slip system in grain i, which is computed based on the classical plastic flow rule:

$$\dot{\gamma}_i^{ss} = \dot{\gamma}_0 \left(\frac{\left|\tau_{\mathrm{i}}^{ss}\right|}{\tau_0^{ss}} \right)^{n-1} \times \left(\frac{\tau_{\mathrm{i}}^{ss}}{\tau_0^{ss}} \right) \tag{10}$$

where τ_{i}^{ss} is the resolved shear stress for the ss slip system in grain i, τ_0^{ss} is the CRSS of the ss slip system, $\dot{\gamma}_0$ is the reference shear rate and n is the strain rate sensitivity exponent. τ_{i}^{ss} is related to the Cauchy stress deviator tensor (S_i) and the Schmid tensor (m_i) as follows:

$$\tau_{\mathrm{i}}^{ss} = \ \mathrm{S}_i : \ m_i^{ss} \tag{11}$$

The overall macroscopic behavior is then obtained by volume-weighted averaging of individual grain responses.

A dedicated scheme was used to study the stress state of surface grains. A schematic representation is shown in Fig. 5. Each grain is a spherical inclusion embedded in a matrix with a macroscopic stiffness accounting for the presence of the free surface. We added 5 layers of infinitely compliant medium in a 100 × 100 × 100 voxels cell. The associated macroscopic stiffness C^{macro} is calculated using the FFT-based model described in Section 3.1 by performing 6 elementary loadings (XX, YY, ZZ, XY, XZ and YZ). The homogenization scheme defined in Eq. (6) was then used.

4. Experimental characterization of deformation mechanisms

4.1. Early slip activity: basal and prismatic slip

The first slip traces were noticed at the 600 MPa step. It corresponds to about 74% of the 0.2% proof stress. At this step, the macroscopic behavior is elastic. This is illustrated on the stress – strain curve displayed in Fig. 2b. The identification of the slip plane reveals basal slip with a high maximum Schmid factor (≈ 0.471). The misorientation between the c-axis of the HCP lattice and the loading direction is 41.5°. Basal slip activity developed with increasing macroscopic stress. The distribution of activated slip systems is plotted with respect to the macroscopic stress in Fig. 6a. The number of new active slip systems was divided by the macroscopic stress increment to dismiss any bias related to its variation during the in-situ test. This plot shows that basal slip is the only deformation mechanism operating in the low macroscopic stress range. The first prismatic slip trace was noticed at the 680 MPa step, which corresponds to about 84% of the 0.2% proof stress. This slip trace is located near a grain boundary and probably results from a stress concentration due to neighboring grains. Significant prismatic slip activity occurred for macroscopic stress higher than 740 MPa. Until 800 MPa, the number of new active slip systems increases sharply. This is mostly related to a development of prismatic slip activity while the activation rate of basal slip systems remains almost constant. The slip system activation rate seemingly decreases for macroscopic stress higher than 810 MPa. This suggests that the increase in plastic strain is mostly accommodated by already active slip systems and generally did not require the operation of additional slip systems. Two deformation regimes can then be distinguished. At low macroscopic stress, only basal slip operates while both basal and prismatic slip are involved in plastic deformation for macroscopic stress higher than 740 MPa. The basal slip dominated and basal and prismatic slip dominated regimes are illustrated in Fig. 6a. The transition between these deformation regimes corresponds to the marked increase in stress relaxation rates shown in Fig. 3b. The magnitude of the stress relaxation seems roughly proportional to the number of active slip systems. It is interesting to note that the number of new active slip systems drops beyond the yield strength.

A total of 170 slip events were analyzed at the end of the test. 134 slip systems were successfully identified, including 48 basal slip systems and 74 prismatic slip systems. Therefore, these slip systems have a dominant contribution to deformation in Ti-6242. Importantly, they operate in α grains belonging to different orientation domains. As shown in Fig. 6b, basal slip is observed in α grains with a misorientation between the c-axis of the HCP lattice and the loading direction in the 13° - 64° range. In contrast, prismatic slip is associated with the 53° - 90° range. As a consequence little overlap exists. These orientation domains are very consistent with prior studies (Bridier et al., 2005; Echlin et al., 2016; Hémery and Villechaise, 2017a, 2017b; Li et al., 2015). Only one or two slip systems were found active in a single α grain. Approximately 4% of slip traces were contained in α grains with multiple slip at the 810 MPa step and 11% at the 840 MPa step, while only single slip was noticed at the 780 MPa step. This observation suggests that interactions between active slip systems are quite rare in this loading regime.

The CRSS values obtained using the self-consistent approach were averaged over each slip mode and are given in table 1. The associated standard deviations are also indicated. The CRSS for basal slip is slightly higher than the CRSS for prismatic slip. As basal

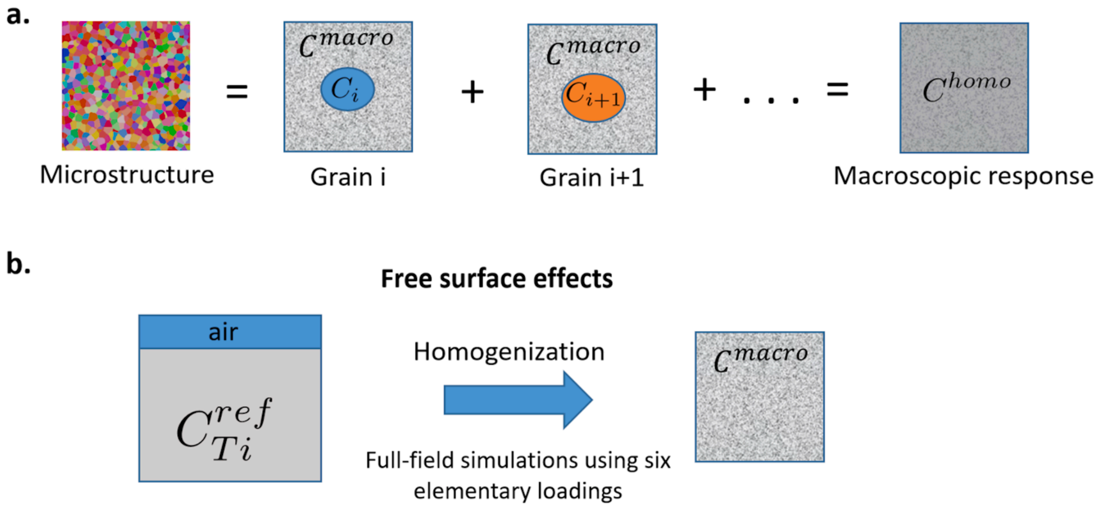

Fig. 5. Schematic representation of a. the classical self-consistent Eshelby-Kröner approach, and b. the modified self-consistent Eshelby-Kröner approach presently employed to simulate free surface effects.

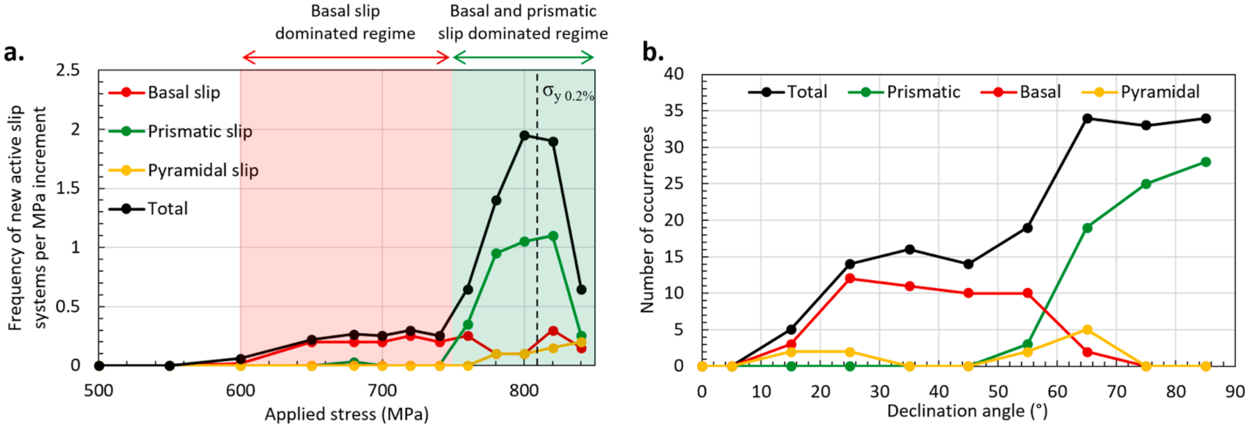

Fig. 6. a. Basal, prismatic and pyramidal slip activation as a function of the applied stress, b. Distribution of basal, prismatic and pyramidal slip with respect to the misorientation between the c-axis of the HCP lattice and the loading direction.

Table 1

Summary of the CRSS values extracted from the experimental data.

Deformation mode	$(0001)\langle 11\bar{2}0\rangle$	$\{10\bar{1}0\}\langle 11\bar{2}0\rangle$	$\{10\bar{1}1\}\langle 11\bar{2}3\rangle$	$\{10\bar{1}2\}\langle 10\bar{1}\bar{1}\rangle$
CRSS (MPa)	332	298	697	≈ 850
Standard deviation (MPa)	47	28	–	–

slip can be activated at a lower macroscopic stress than prismatic slip, significant stress heterogeneity results from the elastic anisotropy of α titanium, which governs the activation sequence of deformation mechanisms. Slightly higher standard deviations were obtained for basal slip than for prismatic slip. Such values account for the effect of the grain neighborhood on the stress state. Indeed, self-consistent models provide an averaged neighborhood effect while experimental observations result from a specific configurations of neighboring grains. α grains where slip traces were detected are plotted with respect to the basal and prismatic Schmid factors in Fig. 7. In this plot, the maximum Schmid factor is considered unless the slip system is active and completely determined using the plane trace. It shows that the active slip system can be quite reliably predicted using the Schmid factor. In addition, a very limited overlap exists considering basal and prismatic slip. However, pyramidal slip, which is further discussed in the dedicated section, was noticed at the interface between both domains. The dashed line represents a Schmid factor ratio equal to the CRSS ratio obtained from the self-consistent approach. An excellent agreement is obtained, showing that (i) the calculated CRSS values are consistent with experimental observations, and (ii) an approach based on Schmid factor ratios provides a proper description of the competition between different slip modes.

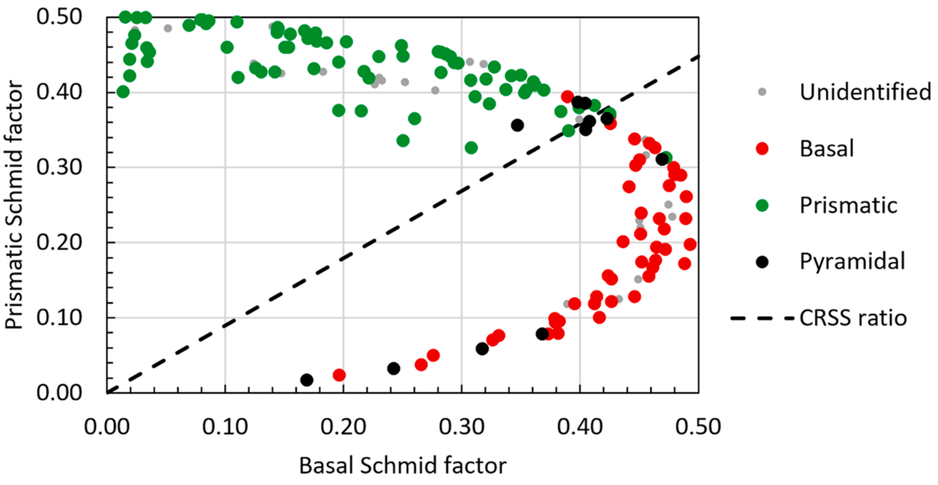

Fig. 7. Analyzed slip traces plotted with respect to the basal and prismatic Schmid factors at the end of the in situ test, suggesting very similar CRSS values for both slip modes but a slightly higher value for basal slip. The presently determined ratio of basal to prismatic CRSS values reveal a good agreement with experimental data.

AFM characterization was carried out on equiaxed α grains with slip traces corresponding to basal or prismatic slip systems. Plastic deformation is accommodated by well-defined and regularly spaced slip lines. This is illustrated in Figs. 8a and 8b. Although slip traces are mostly matching basal or prismatic plane traces, some segments are wavy and do not correspond to any of these planes. Higher magnification images illustrating this feature are shown in Fig. 8c. This observation testifies of frequent cross-slip events. Height profiles were extracted along a path normal to the slip traces and located in the center of the grain. A typical profile is shown in Fig. 9a alongside data processed to extract slip step height and spacing in Figs. 9b and 9c. Three α grains were analyzed for each slip mode. To dismiss bias related to the orientation of the Burgers vector relative to the specimen surface, height values were divided by the magnitude of the Burgers vector component normal to the specimen surface. A single slip system is assumed active with this procedure. Analysis of the curves reveals a higher degree of localization for prismatic slip as steps equivalent to up to approximately 464 dislocations were found for this slip mode versus 170 dislocations for basal slip. This feature is also associated with a higher slip spacing for prismatic slip. A peak detection program with a prominence criterion of 1 nm was used to assess the spacing between slip traces. It is about 0.62 μm for basal slip versus 2.08 μm for prismatic slip within the investigated α grains. The higher degree of localization related to prismatic slip than for basal slip was also noticed using HR-DIC (Lunt et al., 2017).

4.2. $\langle c + a \rangle$ pyramidal slip

The distinction between $\langle \mathrm{a} \rangle$ and $\langle c + a \rangle$ slip directions cannot be achieved using a classical slip traces analysis. Features of $\langle c + a \rangle$ pyramidal slip such as the slip plane and the degree of slip localization were investigated through consideration of a specific crystallographic orientation domain which is unfavorable to $<a>$-type pyramidal slip activity. In the crystallographic orientation domain associated with misorientations between the c-axis and the loading direction lower than 45°, only $\langle c + a \rangle$ pyramidal slip exhibits Schmid factors higher than 0.4. Schmid factor isocontours illustrating this feature can be found in (Echlin et al., 2016; Li et al., 2015). Possible $\langle c + a \rangle$ slip in the remaining orientation domain is discussed in the following paragraph. In the regions of interest followed all along the in situ test, the first evidence of pyramidal slip in an α grain contained in the considered orientation domain was observed at a macroscopic stress of 820 MPa, which corresponds to a plastic strain of 0.3% and 101% of the 0.2% proof stress. Only 4 occurrences were found at the end of the test. Supplementary data was obtained in the additional regions monitored from 810 MPa to the end of the test. To identify the slip plane of $\langle c + a \rangle$ dislocations with the present test conditions, the misorientation between the slip trace and closest calculated plane trace was computed considering both first and second order pyramidal planes. The distribution of values is shown in Fig. 10a. While first order pyramidal planes are always within 5° from the experimental plane trace, a poor agreement is found considering second order pyramidal planes. Therefore, $\langle c + a \rangle$ slip is likely to proceed preferentially on first order pyramidal planes with the applied loading conditions. This feature is consistent with numerous observations reported in the literature (Jones and Hutchinson, 1981a; Ding et al., 2014; Wu and Curtin, 2016).

Active slip systems at the end of the test are plotted with respect to the Schmid factor for basal and $\langle c + a \rangle$ first order pyramidal slip in Fig. 10b. The maximum Schmid factor value that can result in the observed plane trace was considered. If the slip system is not active, the maximum Schmid factor was considered. Only α grains in the orientation domain defined in the previous paragraph were included in this plot. The different slip modes are associated with distinct regions that overlap over a restricted domain: $\langle c + a \rangle$ pyramidal slip occurs with a high Schmid factor (SF) for this slip system (SF > 0.42) and a low SF for basal slip (SF < 0.38). In contrast, basal slip occurs when the SF for $\langle c + a \rangle$ pyramidal slip is low (SF < 0.42) and the SF for basal slip is high (SF > 0.19). Dashed lines showing ratios of pyramidal SF to basal SF are indicated. The domain where both slip modes overlap is located between the 1.3 and 2.5 lines. This provides bounds for CRSS values. A more refined assessment of the CRSS for $\langle c + a \rangle$ pyramidal slip was obtained using SF ratio calculations for each α grain showing basal or pyramidal slip activity as its activation proceeds mostly beyond 0.2% plastic strain. The fraction of basal or $\langle c + a \rangle$ pyramidal slip experimentally identified is plotted in Fig. 10c as a function of the SF ratio. A progressive switch from basal dominated slip at low SF ratios to $\langle c + a \rangle$ pyramidal slip dominated regime at high SF ratios indicates that this parameter is suitable for the description of the transition between both regimes. Evolutions were fitted using an error and a complementary error functions. The resulting curves are shown in Fig. 10c. Activity of both slip systems is equally probable for a SF ratio of

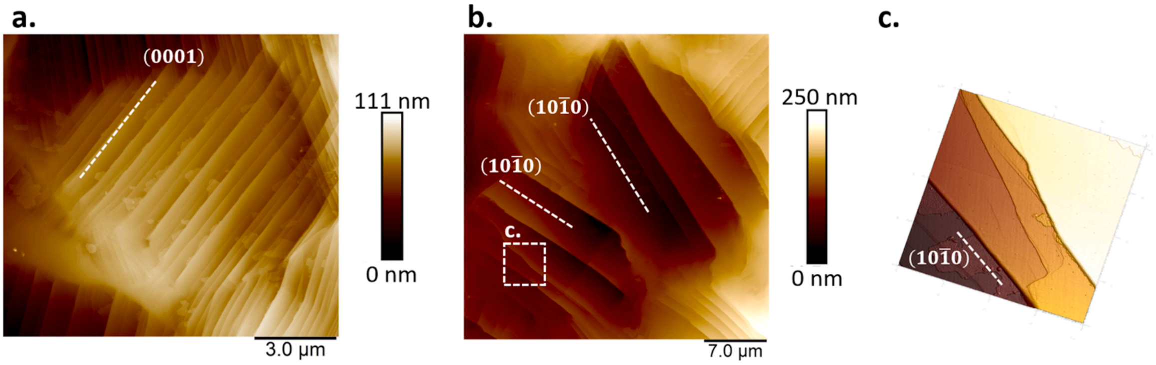

Fig. 8. AFM topography images showing equiaxed α grains deforming via a. basal and b. prismatic slip. c. 3D representation of a subset of the topography image shown in b. demonstrating the occurrence of cross-slip.

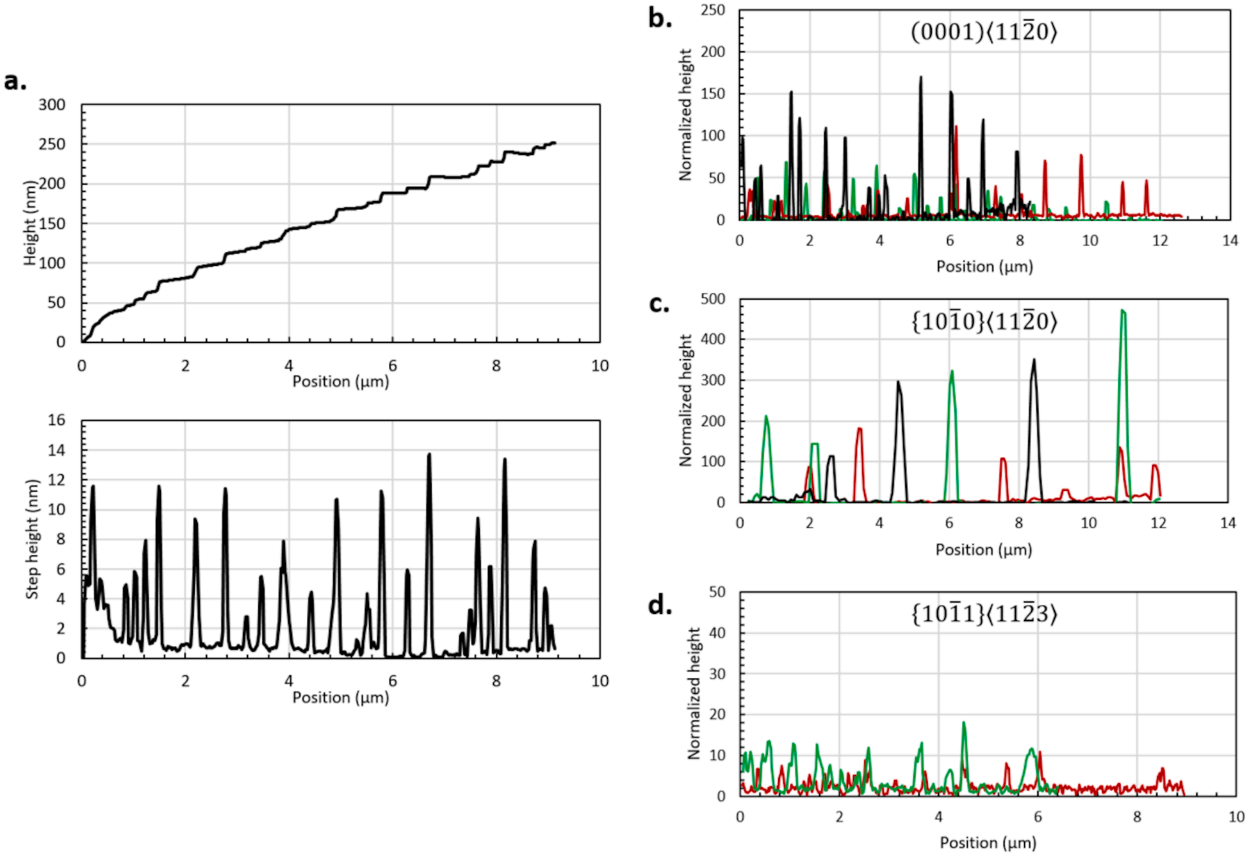

Fig. 9. a. Height profile and subsequent slip step height measurement after plane fitting illustrating the applied procedure, b., c., and d. Normalized height profiles obtained using AFM for basal, prismatic, and pyramidal slip, respectively, indicating the equivalent number of dislocations needed to generate experimentally measured step heights. Colors refer to measurements carried out in different α grains.

about 2.1. The CRSS for $\langle c + a \rangle$ pyramidal slip is thus approximately 2.1 times higher than the CRSS for basal slip. It is noteworthy that the choice of different intervals has not led to a significant change of this value, which lies within the range of frequently reported CRSS ratio for $\langle c + a \rangle$ pyramidal slip (Hémery et al., 2020). Possible $\langle c + a \rangle$ pyramidal slip activity in the orientation domain associated with a misorientation between the c-axis and the loading direction higher than 45° was assessed via estimation of SF ratios in this domain. The ratio of the maximum Schmid factor among $\langle c + a \rangle$ type pyramidal slip systems and the maximum Schmid factor among basal and prismatic slip systems was calculated using 3° steps on the Euler angles. An in-house Matlab script was used for this purpose. The maximum ratio is about 1.30. This reveals that a CRSS for $\langle c + a \rangle$ type pyramidal slip higher than 1.3 times the one for basal or prismatic slip should lead to a lack - or rare occurrences - of $\langle c + a \rangle$ type pyramidal slip activity. As the CRSS ratio is about 2.1, $\langle c + a \rangle$ pyramidal slip activity is very unlikely when the c-axis is deviated from the loading axis by more than 45° and basal or prismatic slip activity would be privileged. It is worth noting that, with this procedure, the basal and prismatic CRSS were considered equal, which is expected to introduce a negligible bias owing to the limited difference.

$\langle c + a \rangle$ type pyramidal slip character was investigated using AFM on different α grains with a misorientation between the c-axis of the HCP lattice and the loading direction lower than 15°. According to the previously reported rationale, this ensures the consideration of $\langle c + a \rangle$ slip. A SEM micrograph showing faint contrasts related to slip traces is reported in Fig. 11a. The corresponding crystallographic orientations are shown in Fig. 11b. An AFM topography image in the same region is reported in Fig. 11c to confirm the presence of slip traces. It reveals that $\langle c + a \rangle$ pyramidal slip is very planar. Normalized step height profiles extracted along a path normal to the slip traces and located in the center of three α grains are shown in Fig. 9d. The AFM profiles appear smoother for $\langle c + a \rangle$ pyramidal slip than for basal and prismatic slip. This results mainly from step heights lower than those corresponding to basal and prismatic slip, as the spacing seems roughly similar. While most steps are approximately equivalent to 50 – 100 dislocations in average for basal slip, they are mostly less than 10 for $\langle c + a \rangle$ pyramidal slip. Higher magnification observations shown in Fig. 11d reveal that slip traces visible in Fig. 11c are actually composed of multiple slip traces arranged in bundles. The height of individual slip steps could be measured in some locations as shown in Fig. 11e. It corresponds to one or two dislocations emerging at the specimen surface, depending on the considered Burgers vector. Indeed, slip can occur along two different slip directions for a given slip plane. While bundles of slip traces are separated by typically 1 μm, slip traces are spaced by less than 100 nm within the bundles. Such features make a quantitative study difficult using techniques other than AFM. The degree of slip localization in grains deforming via $\langle c + a \rangle$ slip is

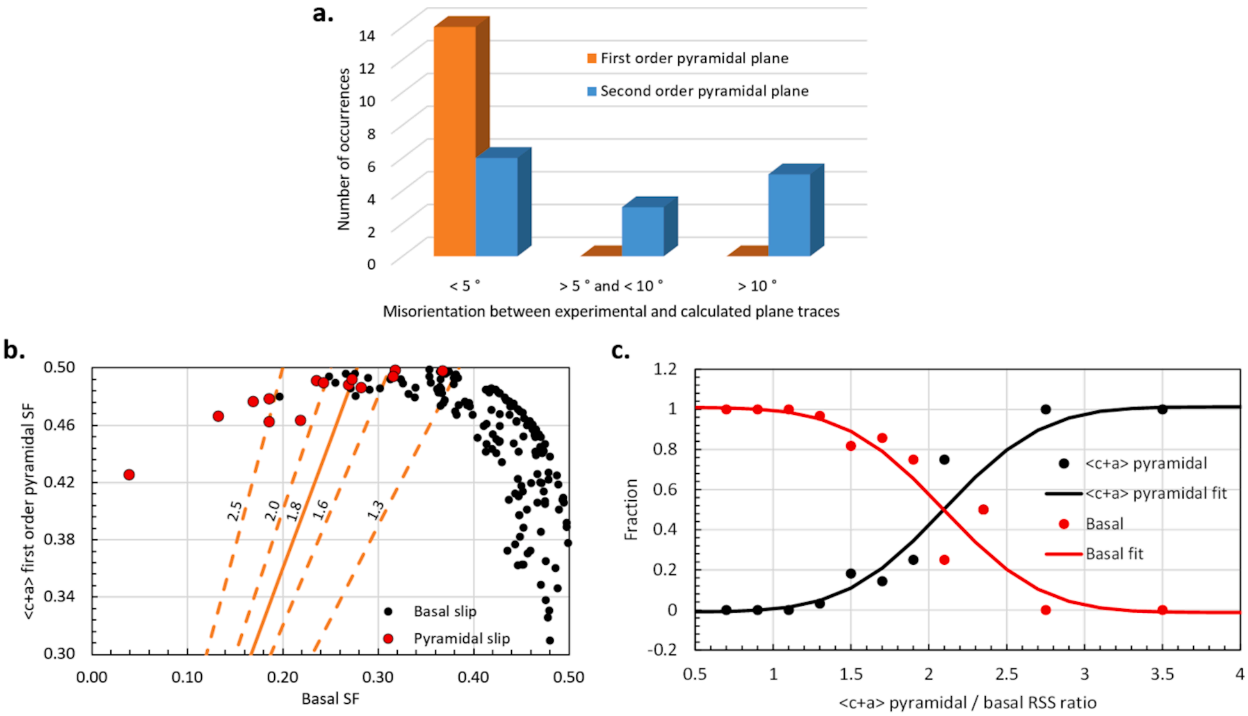

Fig. 10. a. Deviation between slip traces and the closest $\{10\bar{1}1\}$ or $\{11\bar{2}2\}$ plane traces showing that only first-order pyramidal planes can account for experimentally observed slip traces, b. α grains with a misorientation between the c axis of the HCP lattice and the loading direction lower than 45° plotted as a function of the Schmid factors for basal and $\langle c + a \rangle$ first-order pyramidal slip, and c. Distribution of the fraction of basal or $\langle c + a \rangle$ pyramidal slip experimentally identified a function of the SF ratio showing a transition from basal to pyramidal slip with increasing ratios.

therefore lower than for basal or prismatic slip. Examination of micrographs reveals that this difference in strain localization has consequences in terms of deformation behavior. Clusters of $\langle c + a \rangle$ slip bands are coincident with intense slip activity located in neighboring grains. This is illustrated in Fig. 11c. S. Joseph et al. reported activation of dislocation sources in α grains with a low misorientation between the c-axis of the HCP lattice and the loading direction due to dislocation pile-ups in neighboring α grains primarily deforming via prismatic slip (Joseph et al., 2020, 2018). The present observations suggest that strain incompatibilities across grain boundaries generated by incoming basal or prismatic slip is difficult to accommodate via diffuse $\langle c + a \rangle$ slip.

4.3. {10–12} twinning

Twin formation was observed in situ at the 830 MPa step, which corresponds to a plastic strain about 0.5%. While often neglected in Ti - 6 wt.% Al alloys, this observation reveals its operation at low macroscopic strain levels. Micrographs showing this event are presented in Fig. 12. The twin is located in a grain with a very low misorientation between the c axis of the HCP lattice and the loading direction (≈ 2 °). As a consequence, this grain is unfavorably oriented for ⟨a⟩ slip. Orientation relationships between the twin and the parent grain are also shown in Fig. 12d and demonstrate that $\{10\bar{1}2\}\langle 10\bar{1}\bar{1} \rangle$ is the active twinning system. The associated Schmid factor is very high (0.4993) and the twin coincides with an incident slip trace located in the adjacent soft grain which has appeared at the same loading step. The alignment between deformation systems on both sides of the boundary was assessed using the *m'* parameter introduced by Luster and Morris (Luster and Morris, 1995). It is calculated as the product of cosines between slip plane normals and between slip directions. A value of 1 indicates a perfect alignment of deformation systems. The 0.9104 value presently obtained reveals a very good alignment, which is likely to allow slip transfer (Hémery et al., 2018a). This feature agrees well with the role of slip transfer in twin nucleation suggested by Wang et al. using commercial purity titanium (Wang et al., 2009) and suggests a similar behavior for Ti – 6% Al based alloys. Slip traces corresponding to a first-order pyramidal plane appeared on the right-hand side of the parent grain at the 830 MPa step. This feature is shown in Fig. 12e and reveals the concurrent operation of $\langle c + a \rangle$ first order pyramidal slip in the same grain but in a different region. No evidence of $\langle c + a \rangle$ pyramidal slip trace could be evidenced nearby the twin, suggesting that the operation of these two deformation mechanisms is not directly interrelated. The concurrent operation of $\langle c + a \rangle$ slip and twinning in so-called "hard" grains was also observed for higher macroscopic strain levels in a prior study (Lavogiez et al., 2018). This feature may pertain to the difficult accommodation of deformation incompatibilities due to incoming ⟨a⟩ slip by diffuse $\langle c + a \rangle$ slip. The persistent stress concentration as well as microstructure configurations ensuring appropriate geometric compatibility (Lavogiez et al., 2020) likely favor twinning, which also permits deformation of the HCP α phase along the c-axis. Hence, the different characteristics of $\langle c + a \rangle$ slip and twinning such as strain localization and strength appear as key features of this competition. The ratio of the SF for twinning to

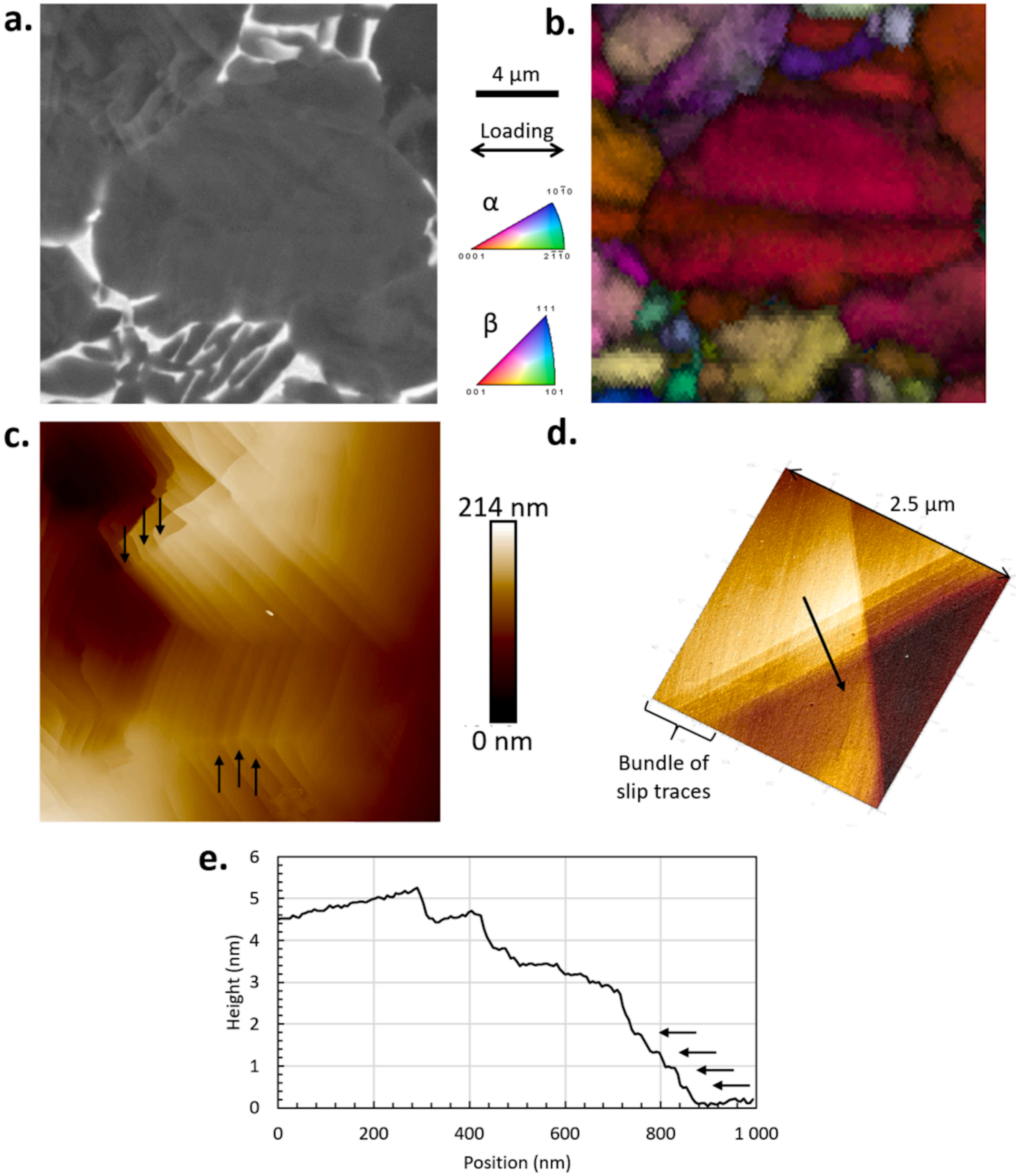

Fig. 11. a. SEM micrograph, b. Inverse pole figure map superimposed with image quality, and c. AFM topography images showing $\langle c + a\rangle$ pyramidal slip traces in the center α grain. Black arrows indicate incoming slip in neighboring grains associated with bundles of pyramidal slip traces. d. Magnified image of a bundle of pyramidal slip traces. The black arrow indicates the height profile shown in e. where arrows show step heights of approximately 0.45 nm.

the SF for $\langle c + a\rangle$ first order pyramidal slip was estimated using the same procedure as employed previously. A value of 1.22 was found and suggests that the CRSS for twinning is likely higher than the one for $\langle c + a\rangle$ first order pyramidal slip. One has to keep in mind that this is a rough estimate because it is derived from a single occurrence. Indeed, the stress state in the vicinity of the grain boundary may significantly differ from the macroscopic stress condition. However, CRSS data for twinning in Ti alloys is so scarce that such estimates can be useful.

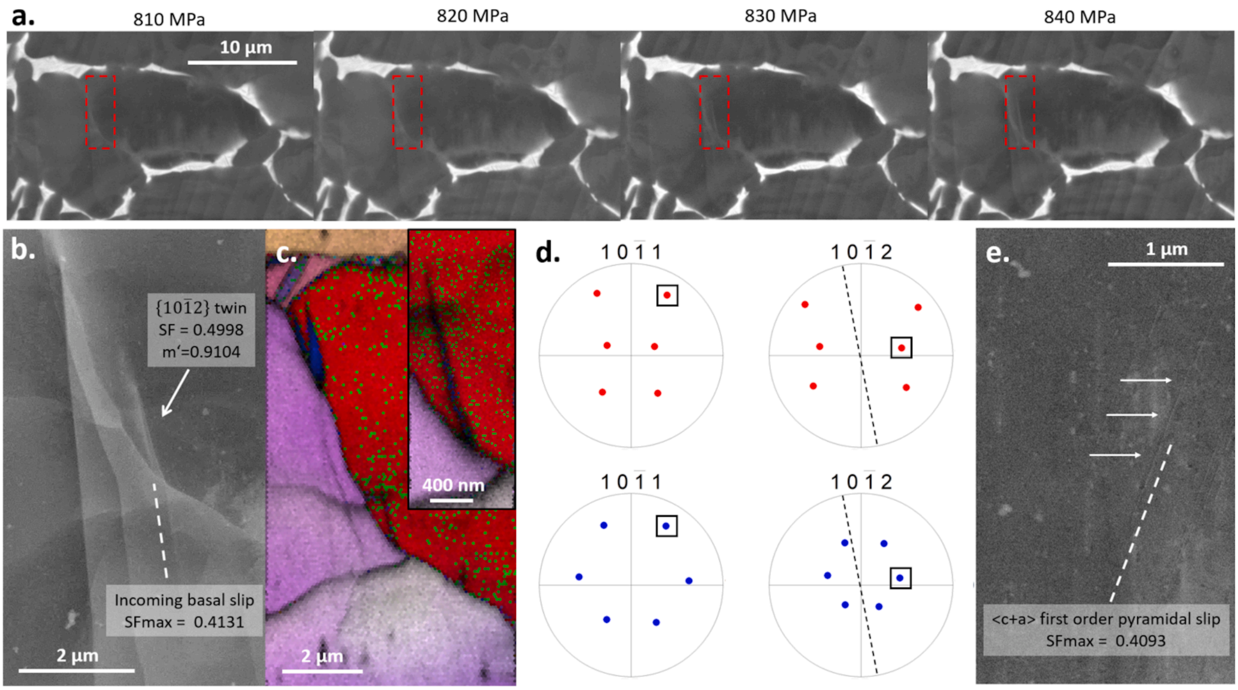

Fig. 12. a. In situ observation of {10–12} twin formation at the 830 MPa step, b. High magnification SEM micrograph at the end of the in situ test showing the presence of a twin and the associated incoming slip band, c. Inverse pole figure map superimposed with the image quality showing the presence of the twin, which is belongs to the $\{10\bar{1}2\}\langle 10\bar{1}\bar{1}\rangle$ twinning system according to the pole figure plots shown in d. and e. slip traces matching a 1st order pyramidal plane in the same α grain.

4.4. $\langle a\rangle$ pyramidal slip

As discussed previously, all pyramidal slip traces in the orientation domain defined by misorientations between the c axis of the HCP lattice and the loading direction higher than 45° are most likely $\langle a\rangle$-type pyramidal slip. This feature is supported by the absence of diffuse slip traces typical of $\langle c+a\rangle$ slip in this orientation domain. The first occurrence of slip trace matching a first order pyramidal plane was observed at the 780 MPa step, which corresponds to 96% of the 0.2% proof stress. At the end of the test, 6 α grains in this orientation domain exhibit slip traces that correspond to first order pyramidal plane traces. It accounts for 3.5% of the total number of slip traces studied, thus suggesting a minor contribution of this slip system to the overall deformation behavior. The Schmid factors of corresponding slip systems were calculated. An average value of 0.222 was obtained. This value is unexpectedly low as 0.423 was obtained for basal and prismatic slip. The Schmid factor distributions for the different slip systems are shown in Fig. 13 and confirm the

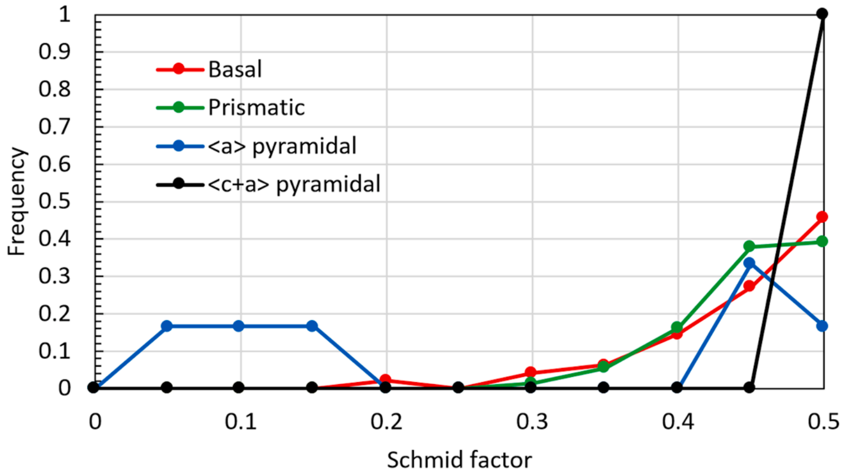

Fig. 13. Schmid factor distribution frequencies for all slip modes presently identified, showing that $\langle a\rangle$ type pyramidal slip does not seem to be associated to high Schmid factors while other slip modes do.

unexpected behavior for $\langle a \rangle$ pyramidal slip. While most occurrences of basal, prismatic and $\langle c + a \rangle$ pyramidal slip are associated to high Schmid factors (> 0.4), a significant number of traces assigned to $\langle a \rangle$ type pyramidal slip exhibit a Schmid factor lower than 0.2. Because of the low expected resolved shear stress, slip is then unlikely to proceed on this identified slip system. Slip trace misidentification possibly occurred. Indeed, frequent cross slip involving basal or prismatic planes, such as highlighted in Fig. 8c, may lead to slip traces that apparently matches a slip system poorly orientated for slip. As no convincing evidence of widespread $\langle a \rangle$ type pyramidal slip activity was obtained, no CRSS value estimation was undertaken.

5. Validation of CRSS values using crystal plasticity simulations

5.1. Determination of parameters for crystal plasticity simulations

CRSS values for basal, prismatic and $\langle c + a \rangle$ type first-order pyramidal slip modes were determined in the previous sections based on grain scale experimental data. Overall, they compare well with values reported in prior studies, which have been recently reviewed (Hémery et al., 2020). $\langle a \rangle$ type pyramidal slip and twinning, which are associated with rare observations, were not included in the CP simulations as a limited contribution to the overall deformation is expected and the degree of uncertainty related to their activity would be high. In particular, the cooperative deformation required to trigger twinning would need further development of standard simulation approaches.

Accurate simulations of the deformation behavior requires the calibration of other parameters involved in the CP model. The strength difference between primary α and transformed β was assessed using nano-indentation. Limited strength difference between microstructural constituents (Chong et al., 2018; Venkatramani et al., 2007) precluded usage of statistical methods to separate the two phases based on the indentation responses such as carried out by Park et al. (Park et al., 2021). Thus, manual identification of the tested microstructure configuration (i.e., primary α, transformed β, or a mixture) was carried out for each indent using SEM micrographs. An example of the acquired micrographs is shown in Fig. 14a. Distributions of hardness measurements are displayed in Fig. 14b. Mean values are reported in table 2. On average, the hardness is slightly lower in transformed β regions than in primary α grains. The difference is about 2.9%. As a linear relationship between strength and hardness is generally assumed (Cahoon et al., 1971; Zhang et al., 2011), a limited strength difference is expected. It was considered in the simulations as follows. Equiaxe α grains were assigned the CRSS values determined in Section 3. In transformed β regions, the CRSS values for basal, prismatic and pyramidal slip were taken as 97.1% of the CRSS value for equiaxe α. Hence, basal, prismatic and $\langle c + a \rangle$ pyramidal slip modes were assigned CRSS values of 323 MPa, 289 MPa and 677 MPa, respectively. It is worth noting that this procedure involved the characterization of the homogenized response. Therefore, an accurate simulation of the behavior of individual lamellas or colonies is not aimed at. A more complex behavior results from size effects and slip transmission processes (Suri et al., 1999; Venkatraman et al., 2022; Zhang et al., 2023). However, a reasonable reproduction of the mechanical constraints exerting on primary α grains, which are considered for CRSS estimation, is expected.

The reference shear strain rate ($\dot{\gamma}_0$) and the strain rate sensitivity exponent (n) were calibrated using macroscopic stress-strain curves obtained using different strain rates. A single $\dot{\gamma}_0$ value is needed for all slip modes. This value is tightly related to the strain rate used in the experiments carried out for CRSS estimation. However, n can substantially differ depending on the considered slip mode (Chatterjee et al., 2017; Xiong et al., 2022; Zhang et al., 2016a). As this study focusses on the quasi-static behavior, a single n value was assigned to all slip modes for the different microstructural elements. To determine both parameters, two tensile tests were carried out using two different strain rates. The elasto-viscoplastic behavior of the material was simulated using the classical Eshelby-Kröner self-consistent model described in Section 3.1. 35% of the particles were assigned CRSS values for transformed β, while

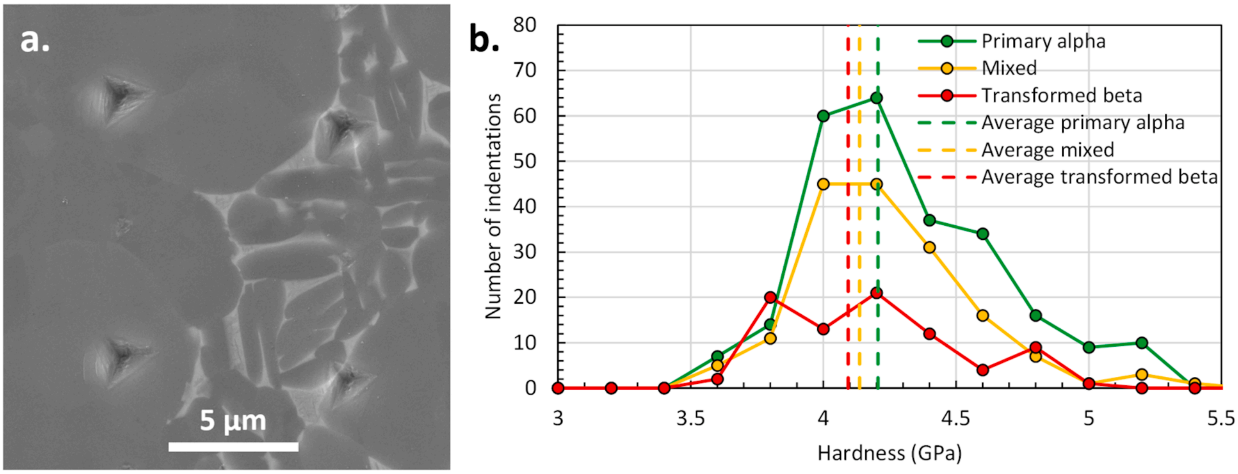

Fig. 14. a. BSE micrograph showing indents, and b. Distribution of hardness values depending on the tested microstructural constituents. Average values are indicated using dashed lines.

Table 2
Average hardness values and associated standard deviations in primary α, transformed β or mixed regions.

Microstructural element	Primary α	Mixed	Transformed β
Average hardness (GPa)	4.21	4.14	4.09
Standard deviation (GPa)	0.36	0.33	0.32

the remaining was considered primary α. Elastic constants from Fisher and Ranken were employed for both types of microstructure elements as the retained β fraction is low (Fisher and Renken, 1964). Stress-strain curves were simulated using $10^{-2} s^{-1}$ and $10^{-4} s^{-1}$ strain rates. A parametric study was performed by varying the values of $\dot{\gamma}_0$ and n within the ranges of $10^{-9} s^{-1}$ to $10^{-6} s^{-1}$ and 10 to 90, respectively. To determine the set of values leading to the best fit, the error between the simulated and experimental behaviors was assessed using the L_2 norm. This norm is calculated as the squared difference between the experimental and simulated yield strength values defined for a 0.2% plastic strain offset, normalized by the experimentally measured yield strength. Resulting values are plotted in Fig. 15a as a function of $\dot{\gamma}_0$ and n values. The best fit was obtained for $\dot{\gamma}_0$ equal to $4.2 \times 10^{-7} s^{-1}$ and n to 47. The order of magnitude of $\dot{\gamma}_0$ is similar to the mean plastic strain rate resulting from in situ testing (i.e., $\sim 10^{-7} s^{-1}$), and n values about 50 were reported in prior studies (Deka et al., 2006). Therefore, such estimates appear sound. The macroscopic stress – strain curves for experiments and optimized parameters are reported in Fig. 15b. An excellent agreement is obtained with the applied set of parameters. Values of the crystal plasticity constitutive model parameters are summarized in table 3.

5.2. Polycrystalline aggregate and crystal plasticity simulations

A polycrystalline aggregate composed of approximately 35,000 equiaxed α grains was generated using the Dream3D software (Groeber and Jackson, 2014). It is shown in Fig. 16a. On average, each α grain contains 5600 voxels. Crystallographic orientations were sampled from the EBSD maps shown in Fig. 1b and include crystallographic orientations of α grains considered in the in situ tensile test. The comparison of textures in the experiment and in the simulation shown in Fig. 16b reveals an excellent agreement. The influence of the low amount of retained β phase was neglected in the elastic regime. Thus, elastic constants determined by Fischer and Ranken, which were also used in simulations involving the self-consistent model, were assigned to all microstructure elements (Fisher and Renken, 1964). CRSS values were assigned as follows: 35% of α grains were considered as transformed β while the remaining fraction was considered as equiaxe α. As mentioned previously, this approach does not aim at simulating the individual behavior of α lamellas or β layers but reproduces the homogenized response in transformed β regions. No slip system hardening was presently considered as no significant influence was observed on slip activation in Ti-6Al-4V (Kasemer et al., 2017). $\dot{\gamma}_0$ and n values established in the previous paragraph were employed. A tensile test was simulated using imposed strain on the simulation cell. A strain rate of $10^{-4} s^{-1}$ was applied. Layers of infinitely compliant medium were added on all other faces to account for the effect of free surfaces. Classically, periodic boundary conditions were then imposed along the boundaries of the cell. The simulation was conducted using our spectral solver with 200 loading steps, lasting 24 h of CPU time. The resulting nominal stress – strain curve is shown in Fig. 16c.

5.3. Comparison of experimental and simulation data

A similar methodology was applied to compare operating deformation mechanisms in the experiment and the simulation. The distribution of active slip modes in primary α grains showing slip activity was extracted at each loading step. In the experiment, slip

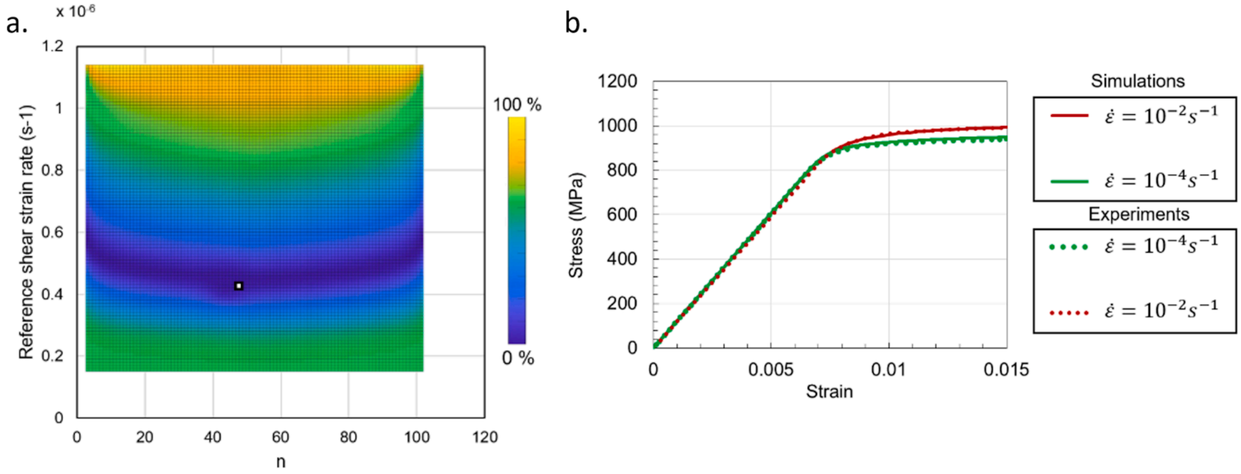

Fig. 15. a. A map of the error calculated between the experimental and simulated stress – strain curves. The white square indicates the minimum error. b. Nominal stress – strain cures obtained using different strain rates from experiments and simulations after calibration of γ_0 and n.

Table 3
Values of the crystal plasticity constitutive model parameters.

	Primary α	Transformed β
τ_c^{Basal} (MPa)	332	323
$\tau_c^{Prismatic}$ (MPa)	298	289
$\tau_c^{Pyramidal}$ (MPa)	697	677
$\dot{\gamma}_0$ (s^{-1})	4.2×10^{-7}	
n	47	

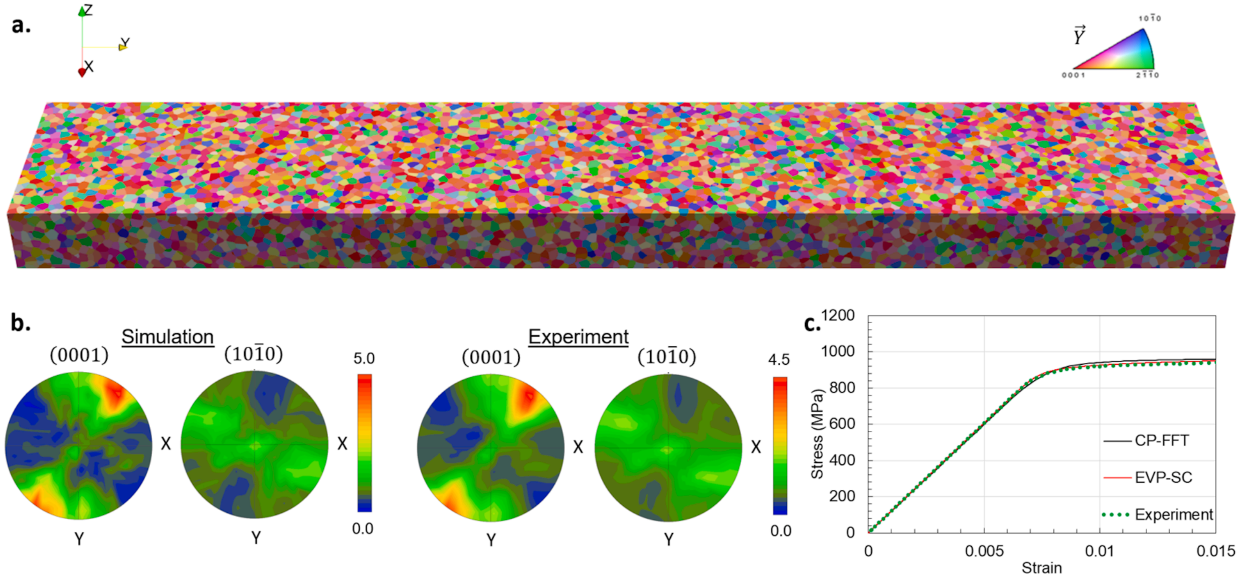

Fig. 16. a. 3D view of the polycrystalline aggregate generated using Dream3D, b. Comparison of texture in the experiment and in the simulation, and c. Comparison of macroscopic stress – strain curves obtained from experiments and different simulation techniques.

activity was detected through the presence of slip traces as described in the previous sections. A shear strain based criterion was employed to determine active slip systems in the simulations. A 0.1% threshold was used to consider a slip system as active. Surface α grains with the same Euler angles were considered for both experiments and simulations to avoid any texture related bias. The percentage of basal, prismatic and pyramidal slip systems in α grains is plotted with respect to the macroscopic stress in Fig. 17. To dismiss any discrepancy related to different strain rates, which is difficult to determine accurately for the experiment, the macroscopic stress magnitudes were expressed as a fraction of the yield strength defined using a 0.2% plastic strain offset. The comparison of experimental and simulated distributions reveals a very good agreement. The simulation properly predicts the early basal slip activity, which is followed by prismatic slip at a macroscopic stress lower than the yield strength. The onset of $\langle c + a \rangle$ pyramidal slip is also well predicted. This reveals that the employed CRSS dataset enables an accurate description of the slip activation sequence. In spite of the approximations and assumptions used, the presently applied determination procedure appears suitable for proper estimation of CRSS datasets.

In spite of the good overall agreement, substantial differences in the distribution of active slip systems are visible in Fig. 17. For example, prismatic slip should prevail at macroscopic stress levels higher than the yield strength according to the experiment. The simulations rather show dominance of basal slip. Multiple causes can be identified to explain these discrepancies. In particular, the CF-FFT model relies on several approximations. In this study, a simple model was chosen to enable a straightforward and reliable identification of most parameters using experimental data from slip traces analysis. However, more advanced CP models would lead to more accurate simulations of deformation. For example, interactions between slip bands and grain boundaries or geometrically necessary dislocations can be accounted for in recent models (Berbenni et al., 2020; F. P. E. Dunne et al., 2007a; Haouala et al., 2020). The simulation of the viscoplastic behavior could be improved as well considering a different rate sensitivity for each deformation mode (Zhang et al., 2016a). In addition, no hardening or softening was presently considered. This feature may impair the agreement with increasing strain. Also, the mechanical behavior of transformed β regions was modeled based on a simple homogenized response captured using indentation, which involves a multiaxial loading. Therefore, some features of the microstructure have not been accurately modeled. For example, an explicit modeling of multi-modal size distribution of α precipitates embedded in β phase was not achieved and the tensile anisotropy associated with α+β colonies was not accounted for (Ashton et al., 2017; Deka et al., 2006). Microtexture heterogeneity was not considered as well. In particular, texture is expected to have major consequences on the distribution of active slip systems. Addressing these limitations constitutes outlooks for future work.

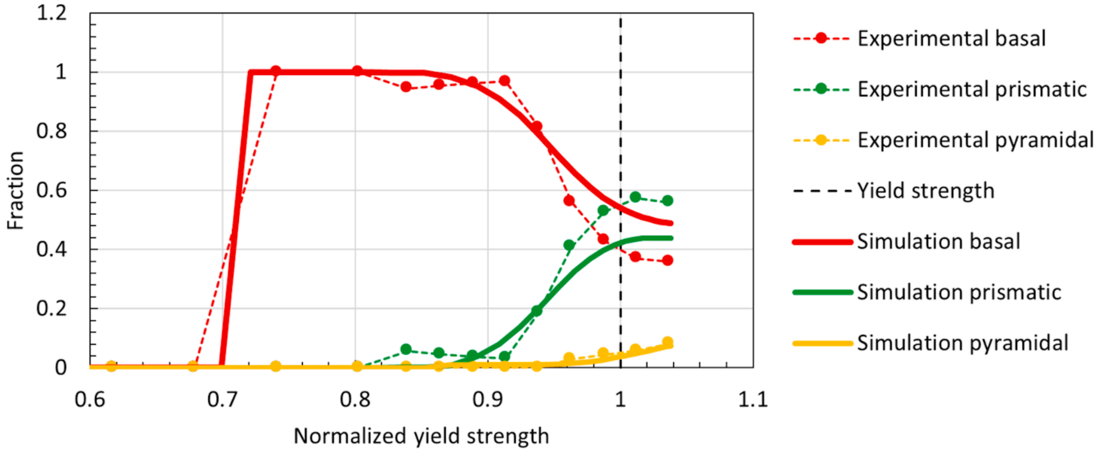

Fig. 17. Distribution of slip modes in primary α grains showing evidence of slip activity at each loading step calculated using experiments and simulations. The macroscopic stress is expressed as a fraction of the yield strength estimated from the in situ tensile test and the CP-FFT simulation, respectively.

Numerous CRSS datasets were established for Ti-6%Al based alloys in prior studies. A non-exhaustive summary is displayed in table 4. The CRSS for $\langle c + a\rangle$ pyramidal slip obtained in the present study lies in the upper range of values reported in the literature. Difficult detection due to the diffuse character, and the competition with basal slip in α grains with their c-axis closely aligned with the loading direction, renders its analysis more intricate than $\langle a\rangle$ slip. In agreement with the presently established dataset, CRSS values reported in the literature testify of similar strengths for basal and prismatic slip. However, different techniques were employed, which result in different magnitudes. For example, single crystal testing include no grain size related strengthening (Hasija et al., 2003a), while micropillar compression may include size effect (Sun et al., 2011). Also, compositions and strain rates can significantly vary and substantially influence CRSS magnitudes. About half of CRSS datasets include CRSS values for basal slip higher than CRSS values for prismatic slip. The present study reveals that this does not necessarily imply that the dataset is inappropriate to describe the early basal slip activity. The origin of the early onset of basal slip pertains to mechanical constraints imposed by neighboring grains. Anisotropic elasticity leads to a stress magnitude higher than average in α grains well-oriented for basal slip while it is lower for α grains well-oriented for prismatic slip (Hémery et al., 2019). Two CP-FFT simulations were carried out using the same methodology as presented above, but isotropic or anisotropic elastic behaviors. The anisotropic deformation was modeled using elastic constants given

Table 4
Summary of CRSS datasets for Ti-6Al based alloys reported in the literature.

Alloy (wt. %)	Basal CRSS (MPa)	Prismatic CRSS (MPa)	$<c + a>$ Pyramidal CRSS (MPa)	Tension / Compression	Reference
Ti-6.6Al	190	200	770	Compression	(Williams et al., 2002)
Ti-6Al	322	320	846	Compression	(Hasija et al., 2003b)
Ti-6Al	260	180	–	Compression	(Xiong et al., 2022)
Ti-7Al	328	342	349	Tension	(Pagan et al., 2017)
Ti-6Al-4V	–	376	441	Tension	(Jones and Hutchinson, 1981b)
Ti-6Al-4V	444	392	631	Compression	(Jones and Hutchinson, 1981b)
Ti-6Al-4V	330	396	561	Tension	(Dawson et al., 2018)
Ti-6Al-4V	353	397	593	Tension	(Song et al., 2008)
Ti-6Al-4V	290	320	440	Tension	(Stapleton et al., 2008)
Ti-6Al-4V	385	410	430	Tension	(Stapleton et al., 2008)
Ti-6Al-4V	420	370	590	Tension	(Bridier et al., 2009)
Ti-6Al-4V	350	275	570	Both	(Smith et al., 2018b)
Ti-6Al-4V	494	395	494	Tension	(Medina Perilla and Gil Sevillano, 1995)
Ti-6Al-4V	513	–	612	Compression	(Medina Perilla and Gil Sevillano, 1995)
Ti-6Al-4V	393	349	–	Compression	(Liu et al., 2021)
Ti-6Al-4V	338	352	–	Tension	(Hémery et al., 2017b)
Ti-6Al-4V	340	231	804	Compression	(Castillo et al., 2021)
Ti-6242	342	221	1150	Compression	(Castillo et al., 2021)
Ti-6242	270	240	–	Compression	(Zhang et al., 2016c)
Ti-6242	385	365	640	Tension	(Deka et al., 2006)
Ti-6242	430	465	760	Compression	(Deka et al., 2006)
Ti-6242	335	364	–	Tension	(Hémery and Villechaise, 2017c)
Ti-6246	362	410	–	Tension	(Hémery and Villechaise, 2017c)

in Section 2.4 while isotropic elasticity involved a Young's modulus of 115 GPa and Poisson's ratio of 0.325 (Welsch et al., 1993). The distribution of active slip modes is reported in Fig. 18 for both conditions. Prismatic slip is active at lower macroscopic stress than basal slip considering an isotropic elasticity framework while the opposite trend exists for anisotropic elasticity. In agreement, CRSS values for basal and prismatic slip would be 308 and 344 MPa respectively considering experimental data alongside a macroscopic stress state, such as experienced for isotropic elasticity (i.e., CRSS values calculated using the Schmid factor instead of the stress state from the self-consistent method). Therefore, compatibility between adjacent microstructural constituents plays a key role determining the early basal slip activity, which has been found critical regarding fatigue properties for example.

6. Conclusions

In situ SEM monitoring of deformation mechanisms was performed on a Ti-6Al-2Sn-4Zr-2Mo specimen during tensile loading. The activation of different deformation modes was investigated at low strain using slip traces analysis and EBSD. Complementary characterization of the slip character was carried out using AFM. Finally, a crystal plasticity model was calibrated using extracted information to simulate the onset of slip activity. Main conclusions were drawn as follows:

- Basal slip operates at low macroscopic stress and prismatic slip is activated next, still below the conventional yield strength. No convincing evidence of significant $\langle a\rangle$-type pyramidal slip activity was obtained in the investigated strain regime. $\langle c + a\rangle$-type pyramidal slip proceeds along first-order pyramidal planes mostly beyond the 0.2% proof stress. Twinning was also detected at a plastic strain level about 0.5% and results from compatible slip activity in a neighboring grain.
- Creep / relaxation kinetics are lower in the macroscopic stress range involving basal slip only. A pronounced increase appears with the progressive operation of prismatic slip. The reduction in fraction of elastically deforming materials is believed to be a key feature.
- The degree of slip localization within α grains is higher for prismatic slip than for basal slip. Also, it is higher for $\langle a\rangle$ slip than for $\langle c + a\rangle$ slip. In particular, accommodation of strain incompatibilities induced by $\langle a\rangle$ slip across grain boundaries is difficult via diffuse $\langle c + a\rangle$ slip. $\langle c + a\rangle$ slip is also more planar than $\langle a\rangle$ slip, which involves frequent occurrences of cross slip.
- A set of initial CRSS values was derived from the slip traces analysis and subsequently validated using CP-FFT simulations. In spite of approximations and hypothesis, the applied procedure resulted in an accurate prediction the sequential activation of the various slip modes.
- The CRSS for basal slip (332 MPa) is slightly higher than the CRSS for prismatic slip (298 MPa) and lower than the CRSS for $\langle c + a\rangle$ pyramidal slip (697 MPa). Elastic anisotropy is responsible for the early activation of basal slip. A rough estimate of the CRSS for twinning was provided (≈ 850 MPa).

CRediT authorship contribution statement

S. Hémery: Writing – original draft, Visualization, Validation, Supervision, Methodology, Investigation, Formal analysis, Data curation, Conceptualization. **A. Naït-Ali:** Writing – review & editing, Visualization, Methodology, Investigation. **O. Smerdova:** Writing – review & editing, Investigation. **C. Tromas:** Writing – review & editing, Visualization, Investigation, Data curation.

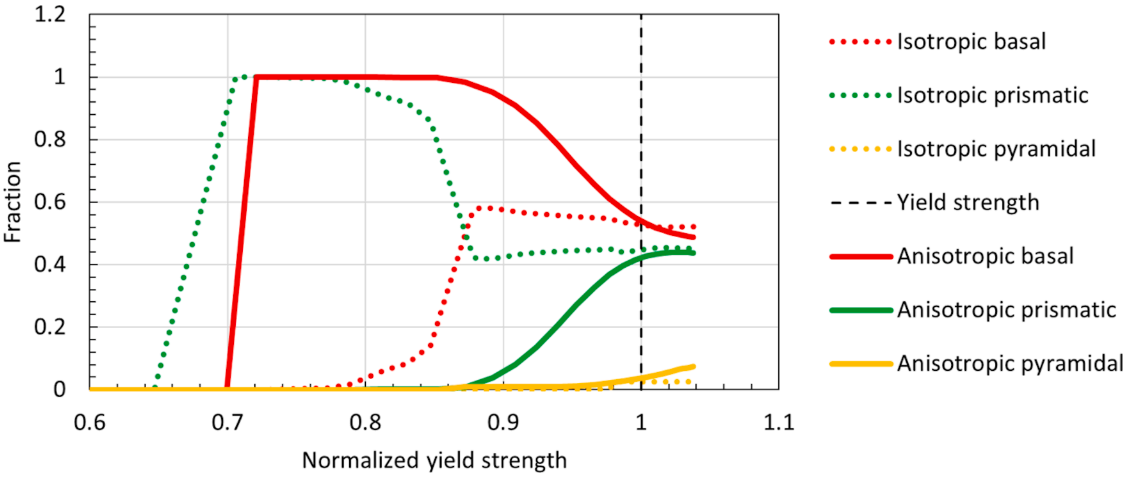

Fig. 18. Distribution of slip modes in primary α grains at each loading step calculated considering isotropic or anisotropic elasticity. The elastic behavior determines the activation sequence of deformation mechanisms.

Declaration of competing interest

The authors declare that they have no known competing financial interests or personal relationships that could have appeared to influence the work reported in this paper.

Data availability

Data will be made available on request.

References

Abdolvand, H., Wright, J., Wilkinson, A.J., 2018. Strong grain neighbour effects in polycrystals. Nat. Commun. 9, 171. https://doi.org/10.1038/s41467-017-02213-9.

Ahmadikia, B., Kumar, M.A., Beyerlein, I.J., 2021. Effect of neighboring grain orientation on strain localization in slip bands in HCP materials. Int. J. Plast. 144, 103026 https://doi.org/10.1016/j.ijplas.2021.103026.

Ashton, P.J., Jun, T.S., Zhang, Z., Britton, T.B., Harte, A.M., Leen, S.B., Dunne, F.P.E., 2017. The effect of the beta phase on the micromechanical response of dual-phase titanium alloys. Int. J. Fatigue 100, 377–387. https://doi.org/10.1016/j.ijfatigue.2017.03.020.

Barkia, B., Doquet, V., Couzinié, J.P., Guillot, I., Héripré, E., 2015. In situ monitoring of the deformation mechanisms in titanium with different oxygen contents. Materials Science and Engineering: A 636, 91–102. https://doi.org/10.1016/j.msea.2015.03.044.

Berbenni, S., Taupin, V., Lebensohn, R.A., 2020. A fast Fourier transform-based mesoscale field dislocation mechanics study of grain size effects and reversible plasticity in polycrystals. J. Mech. Phys. Solids. 135, 103808 https://doi.org/10.1016/j.jmps.2019.103808.

Bhattacharyya, J.J., Nair, S., Pagan, D.C., Tari, V., Lebensohn, R.A., Rollett, A.D., Agnew, S.R., 2021. Elastoplastic transition in a metastable β-Titanium alloy, Timetal-18 – An in-situ synchrotron X-ray diffraction study. Int. J. Plast. 139, 102947 https://doi.org/10.1016/j.ijplas.2021.102947.

Bourdin, F., Stinville, J.C., Echlin, M.P., Callahan, P.G., Lenthe, W.C., Torbet, C.J., Texier, D., Bridier, F., Cormier, J., Villechaise, P., Pollock, T.M., Valle, V., 2018. Measurements of plastic localization by heaviside-digital image correlation. Acta Mater. 157, 307–325. https://doi.org/10.1016/j.actamat.2018.07.013.

Brandes, M.C., Mills, M.J., Williams, J.C., 2010. The Influence of Slip Character on the Creep and Fatigue Fracture of an α Ti-Al Alloy. Metall. Mater. Trans. A 41, 3463–3472. https://doi.org/10.1007/s11661-010-0407-z.

Bretin, R., Levesque, M., Bocher, P., 2019. Neighborhood effect on the strain distribution in linearly elastic polycrystals: Part 1 – Finite element study of the interaction between grains. Int. J. Solids. Struct. 176–177, 36–48. https://doi.org/10.1016/j.ijsolstr.2019.05.015.

Bridier, F., McDowell, D.L., Villechaise, P., Mendez, J., 2009. Crystal plasticity modeling of slip activity in Ti–6Al–4 V under high cycle fatigue loading. Int. J. Plast. 25, 1066–1082. https://doi.org/10.1016/j.ijplas.2008.08.004.

Bridier, F., Villechaise, P., Mendez, J., 2005. Analysis of the different slip systems activated by tension in a α/β titanium alloy in relation with local crystallographic orientation. Acta Mater. 53, 555–567. https://doi.org/10.1016/j.actamat.2004.09.040.

Cahoon, J.R., Broughton, W.H., Kutzak, A.R., 1971. The determination of yield strength from hardness measurements. Metall. Trans. 2, 1979–1983. https://doi.org/10.1007/BF02913433.

Cappola, J., Stinville, J.C., Charpagne, M.A., Callahan, P.G., Echlin, M.P., Pollock, T.M., Pilchak, A., Kasemer, M., 2020. On the Localization of Plastic Strain in Microtextured Regions of Ti-6Al-4 V. Acta Mater. 116492 https://doi.org/10.1016/j.actamat.2020.116492.

Castany, P., Pettinari-Sturmel, F., Crestou, J., Douin, J., Coujou, A., 2007. Experimental study of dislocation mobility in a Ti–6Al–4 V alloy. Acta Mater. 55, 6284–6291. https://doi.org/10.1016/j.actamat.2007.07.032.

Castillo, A.R., Venkatraman, A., Kalidindi, S.R., 2021. Mechanical Responses of Primary-α Ti Grains in Polycrystalline Samples: Part II—Bayesian Estimation of Crystal-Level Elastic-Plastic Mechanical Properties from Spherical Indentation Measurements. Integr. Mater. Manuf. Innov. 10, 99–114. https://doi.org/10.1007/s40192-021-00204-9.

Chakraborty, A., Zhang, C., Balachandran, S., Bieler, T.R., Eisenlohr, P., 2020. Assessment of surface and bulk-dominated methodologies to measure critical resolved shear stresses in hexagonal materials. Acta Mater. 184, 241–253. https://doi.org/10.1016/j.actamat.2019.11.023.

Charpagne, M.A., Stinville, J.C., Callahan, P.G., Texier, D., Chen, Z., Villechaise, P., Valle, V., Pollock, T.M., 2020. Automated and quantitative analysis of plastic strain localization via multi-modal data recombination. Mater. Charact. 163, 110245 https://doi.org/10.1016/j.matchar.2020.110245.

Chatterjee, K., Ko, J.Y.P., Weiss, J.T., Philipp, H.T., Becker, J., Purohit, P., Gruner, S.M., Beaudoin, A.J., 2017. Study of residual stresses in Ti-7Al using theory and experiments. J. Mech. Phys. Solids. 109, 95–116. https://doi.org/10.1016/j.jmps.2017.08.008.

Chong, Y., Bhattacharjee, T., Park, M.H., Shibata, A., Tsuji, N., 2018. Factors determining room temperature mechanical properties of bimodal microstructures in Ti-6Al-4 V alloy. Materials Science and Engineering: A 730, 217–222. https://doi.org/10.1016/j.msea.2018.06.019.

Dawson, P.R., Boyce, D.E., Park, J.S., Wielewski, E., Miller, M.P., 2018. Determining the strengths of HCP slip systems using harmonic analyses of lattice strain distributions. Acta Mater. 144, 92–106. https://doi.org/10.1016/j.actamat.2017.10.032.

Deka, D., Joseph, D.S., Ghosh, S., Mills, M.J., 2006. Crystal plasticity modeling of deformation and creep in polycrystalline Ti-6242. Metall. Mater. Trans. A 37, 1371–1388. https://doi.org/10.1007/s11661-006-0082-2.

Dhekne, P.P., Vermeij, T., Devulapalli, V., Jadhav, S.D., Hoefnagels, J.P.M., Geers, M.G.D., Vanmeensel, K., 2023. Micro-mechanical deformation behavior of heat-treated laser powder bed fusion processed Ti-6Al-4 V. Scr. Mater. 233, 115505 https://doi.org/10.1016/j.scriptamat.2023.115505.

Dichtl, C., Lunt, D., Atkinson, M., Thomas, R., Plowman, A., Barzdajn, B., Sandala, R., da Fonseca, J.Q., Preuss, M., 2022. Slip activity during low-stress cold creep deformation in a near-α titanium alloy. Acta Mater. 229, 117691 https://doi.org/10.1016/j.actamat.2022.117691.

Ding, R., Gong, J., Wilkinson, A.J., Jones, I.P., 2014. ⟨c+a⟩ Dislocations in deformed Ti–6Al–4 V micro-cantilevers. Acta Mater. 76, 127–134. https://doi.org/10.1016/j.actamat.2014.05.010.

Dunne, F.P.E., Rugg, D., Walker, A., 2007a. Lengthscale-dependent, elastically anisotropic, physically-based hcp crystal plasticity: Application to cold-dwell fatigue in Ti alloys. Int. J. Plast. 23, 1061–1083. https://doi.org/10.1016/j.ijplas.2006.10.013.

Dunne, F.P.E., Walker, A., Rugg, D., 2007b. A systematic study of hcp crystal orientation and morphology effects in polycrystal deformation and fatigue. Proceedings of the Royal Society A: Mathematical, Physical and Engineering Sciences 463, 1467–1489. https://doi.org/10.1098/rspa.2007.1833.

Echlin, M.P., Stinville, J.C., Miller, V.M., Lenthe, W.C., Pollock, T.M., 2016. Incipient slip and long range plastic strain localization in microtextured Ti-6Al-4 V titanium. Acta Mater. 114, 164–175. https://doi.org/10.1016/j.actamat.2016.04.057.

Eshelby, J.D., 1957. The Determination of the Elastic Field of an Ellipsoidal Inclusion, and Related Problems. Proc. R. Soc. Lond. Math. Phys. Sci. 241, 376–396.

Esqué-de los Ojos, D., Nguyen, C.T., Orozco-Caballero, A., Timár, G., Quinta da Fonseca, J., 2018. Back-stresses and geometrical hardening as competing mechanisms enhancing ductility in HCP metals. Materials Science and Engineering: A 729, 37–47. https://doi.org/10.1016/j.msea.2018.05.046.

Fisher, E., Renken, C., 1964. Single-Crystal Elastic Moduli and the hcp –>bcc Transformation in Ti, Zr, and Hf. 10.1103/PHYSREV.135.A482.

Fitzner, A., Prakash, D.G.L., da Fonseca, J.Q., Thomas, M., Zhang, S.Y., Kelleher, J., Manuel, P., Preuss, M., 2016. The effect of aluminium on twinning in binary alpha-titanium. Acta Mater. 103, 341–351. https://doi.org/10.1016/j.actamat.2015.09.048.

Groeber, M.A., Jackson, M.A., 2014. DREAM.3D: A Digital Representation Environment for the Analysis of Microstructure in 3D. Integr. Mater. Manuf. Innov. 3, 56–72. https://doi.org/10.1186/2193-9772-3-5.

Haouala, S., Alizadeh, R., Bieler, T.R., Segurado, J., LLorca, J., 2020. Effect of slip transmission at grain boundaries in Al bicrystals. Int. J. Plast. 126, 102600 https://doi.org/10.1016/j.ijplas.2019.09.006.

Hasija, V., Ghosh, S., Mills, M.J., Joseph, D.S., 2003a. Deformation and creep modeling in polycrystalline Ti–6Al alloys. Acta Mater. 51, 4533–4549. https://doi.org/10.1016/S1359-6454(03)00289-1.

Hasija, V., Ghosh, S., Mills, M.J., Joseph, D.S., 2003b. Deformation and creep modeling in polycrystalline Ti–6Al alloys. Acta Mater. 51, 4533–4549. https://doi.org/10.1016/S1359-6454(03)00289-1.

Hémery, S., Dang, T., Signor, L., Villechaise, P., 2018b. Influence of Microtexture on Early Plastic Slip Activity in Ti-6Al-4 V Polycrystals. Metall. Mater. Trans. A 49, 2048–2056. https://doi.org/10.1007/s11661-018-4569-4.

Hémery, S., Naït-Ali, A., Guéguen, M., Wendorf, J., Polonsky, A.T., Echlin, M.P., Stinville, J.C., Pollock, T.M., Villechaise, P., 2019. A 3D analysis of the onset of slip activity in relation to the degree of micro-texture in Ti–6Al–4 V. Acta Mater. 181, 36–48. https://doi.org/10.1016/j.actamat.2019.09.028.

Hémery, S., Nait-Ali, A., Villechaise, P., 2017a. Combination of in-situ SEM tensile test and FFT-based crystal elasticity simulations of Ti-6Al-4 V for an improved description of the onset of plastic slip. Mechanics of Materials 109, 1–10. https://doi.org/10.1016/j.mechmat.2017.03.013.

Hémery, S., Nait-Ali, A., Villechaise, P., 2017b. Combination of in-situ SEM tensile test and FFT-based crystal elasticity simulations of Ti-6Al-4 V for an improved description of the onset of plastic slip. Mech. Mater. 109, 1–10. https://doi.org/10.1016/j.mechmat.2017.03.013.

Hémery, S., Villechaise, P., 2019. In situ EBSD investigation of deformation processes and strain partitioning in bi-modal Ti-6Al-4 V using lattice rotations. Acta Mater. 171, 261–274. https://doi.org/10.1016/j.actamat.2019.04.033.

Hémery, S., Nizou, P., Villechaise, P., 2018a. In situ SEM investigation of slip transfer in Ti-6Al-4V: Effect of applied stress. Materials Science and Engineering: A 709, 277–284. https://doi.org/10.1016/j.msea.2017.10.058.

Hémery, S., Villechaise, P., 2017a. On the influence of ageing on the onset of plastic slip in Ti-6Al-4 V at room temperature: Insight on dwell fatigue behavior. Scr. Mater. 130, 157–160. https://doi.org/10.1016/j.scriptamat.2016.11.042.

Hémery, S., Villechaise, P., 2017b. Comparison of slip system activation in Ti-6Al-2Sn-4Zr-2Mo and Ti-6Al-2Sn-4Zr-6Mo under tensile, fatigue and dwell-fatigue loadings. Materials Science and Engineering: A 697, 177–183. https://doi.org/10.1016/j.msea.2017.05.021.

Hémery, S., Villechaise, P., 2017c. Comparison of slip system activation in Ti-6Al-2Sn-4Zr-2Mo and Ti-6Al-2Sn-4Zr-6Mo under tensile, fatigue and dwell-fatigue loadings. Mater. Sci. Eng. A-Struct. 697, 177–183. https://doi.org/10.1016/j.msea.2017.05.021.

Hémery, S., Villechaise, P., Banerjee, D., 2020. Microplasticity at Room Temperature in α/β Titanium Alloys. Metall. Mater. Trans. A 51, 4931–4969. https://doi.org/10.1007/s11661-020-05945-4.

Hu, H., Briffod, F., Shiraiwa, T., Enoki, M., 2023. Automated slip system identification and strain analysis framework using high-resolution digital image correlation data: Application to a bimodal Ti-6Al-4 V alloy. Int. J. Plast. 166, 103618 https://doi.org/10.1016/j.ijplas.2023.103618.

Imam, M.A., Gilmore, C.M., 1979. Room temperature creep of Ti-6AI-4 V. Metall. Mater. Trans. A 10, 419–425. https://doi.org/10.1007/BF02697068.

Jones, I.P., Hutchinson, W.B., 1981a. Stress-state dependence of slip in Titanium-6Al-4 V and other H.C.P. metals. Acta Metallurgica 29, 951–968. https://doi.org/10.1016/0001-6160(81)90049-3.

Jones, I.P., Hutchinson, W.B., 1981b. Stress-state dependence of slip in Titanium-6Al-4 V and other H.C.P. metals. Acta Metallurgica 29, 951–968. https://doi.org/10.1016/0001-6160(81)90049-3.

Joseph, S., Joseph, K., Lindley, T.C., Dye, D., 2020. The role of dwell hold on the dislocation mechanisms of fatigue in a near alpha titanium alloy. Int. J. Plast. 131, 102743 https://doi.org/10.1016/j.ijplas.2020.102743.

Joseph, S., Lindley, T.C., Dye, D., 2018. Dislocation interactions and crack nucleation in a fatigued near-alpha titanium alloy. Int. J. Plast. 110, 38–56. https://doi.org/10.1016/j.ijplas.2018.06.009.

Kapoor, K., Ravi, P., Naragani, D., Park, J.S., Almer, J.D., Sangid, M.D., 2020. Strain rate sensitivity, microstructure variations, and stress-assisted $\beta \rightarrow \alpha''$ phase transformation investigation on the mechanical behavior of dual-phase titanium alloys. Mater. Charact. 166, 110410 https://doi.org/10.1016/j.matchar.2020.110410.

Kasemer, M., Echlin, M.P., Stinville, J.C., Pollock, T.M., Dawson, P., 2017. On slip initiation in equiaxed α/β Ti-6Al-4 V. Acta Mater. 136, 288–302. https://doi.org/10.1016/j.actamat.2017.06.059.

Kawano, Y., Sato, M., Mayama, T., Mitsuhara, M., Yamasaki, S., 2020. Quantitative evaluation of slip activity in polycrystalline α-titanium considering non-local interactions between crystal grains. Int. J. Plast. 127, 102638 https://doi.org/10.1016/j.ijplas.2019.12.001.

Khan, A.S., Sung Suh, Y., Kazmi, R., 2004. Quasi-static and dynamic loading responses and constitutive modeling of titanium alloys. Int. J. Plast. 20, 2233–2248. https://doi.org/10.1016/j.ijplas.2003.06.005.

Kröner, E., 1958. Berechnung der elastischen Konstanten des Vielkristalls aus den Konstanten des Einkristalls. Z. Physik 151, 504–518. https://doi.org/10.1007/BF01337948.

Lagattu, F., Bridier, F., Villechaise, P., Brillaud, J., 2006. In-plane strain measurements on a microscopic scale by coupling digital image correlation and an in situ SEM technique. Mater. Charact. 56, 10–18. https://doi.org/10.1016/j.matchar.2005.08.004.

Lavogiez, C., Hémery, S., Villechaise, P., 2018. Concurrent operation of $\langle c + a\rangle$ slip and twinning under cyclic loading of Ti-6Al-4 V. Scr. Mater. 157, 30–33. https://doi.org/10.1016/j.scriptamat.2018.07.033.

Lavogiez, C., Hémery, S., Villechaise, P., 2020. Analysis of deformation mechanisms operating under fatigue and dwell-fatigue loadings in an α/β titanium alloy. Int. J. Fatigue 131, 105341. https://doi.org/10.1016/j.ijfatigue.2019.105341.

Lebensohn, R.A., Kanjarla, A.K., Eisenlohr, P., 2012. An elasto-viscoplastic formulation based on fast Fourier transforms for the prediction of micromechanical fields in polycrystalline materials. Int. J. Plast. 32–33, 59–69. https://doi.org/10.1016/j.ijplas.2011.12.005.

Lhadi, S., Berbenni, S., Gey, N., Richeton, T., Germain, L., 2018. Micromechanical modeling of the effect of elastic and plastic anisotropies on the mechanical behavior of β-Ti alloys. Int. J. Plast. 109, 88–107. https://doi.org/10.1016/j.ijplas.2018.05.010.

Li, H., Boehlert, C.J., Bieler, T.R., Crimp, M.A., 2015. Examination of the distribution of the tensile deformation systems in tension and tension-creep of Ti-6Al-4 V (wt.%) at 296 K and 728 K. Philosophical Magazine 95, 691–729. https://doi.org/10.1080/14786435.2014.1001459.

Li, H., Mason, D.E., Bieler, T.R., Boehlert, C.J., Crimp, M.A., 2013. Methodology for estimating the critical resolved shear stress ratios of α-phase Ti using EBSD-based trace analysis. Acta Mater. 61, 7555–7567. https://doi.org/10.1016/j.actamat.2013.08.042.

Liu, Y., Adande, S., Britton, T.B., Dunne, F.P.E., 2021. Cold dwell fatigue analyses integrating crystal-level strain rate sensitivity and microstructural heterogeneity. Int. J. Fatigue 106398. https://doi.org/10.1016/j.ijfatigue.2021.106398.

Liu, Y., Dunne, F.P.E., 2020. The Mechanistic Link between Macrozones and Dwell Fatigue in Titanium Alloys. Int. J. Fatigue 105971. https://doi.org/10.1016/j.ijfatigue.2020.105971.

Lunt, D., Busolo, T., Xu, X., Quinta da Fonseca, J., Preuss, M., 2017. Effect of nanoscale α2 precipitation on strain localisation in a two-phase Ti-alloy. Acta Mater. 129, 72–82. https://doi.org/10.1016/j.actamat.2017.02.068.

Luster, J., Morris, M.A., 1995. Compatibility of deformation in two-phase Ti-Al alloys: Dependence on microstructure and orientation relationships. Metall. Mater. Trans. A 26, 1745–1756. https://doi.org/10.1007/BF02670762.

Lütjering, Gerd, Williams, James C., 2007. Titanium. Springer, Berlin, Heidelberg.

Ma, Y., Xue, Q., Wang, H., Huang, S., Qiu, J., Feng, X., Lei, J., Yang, R., 2017. Deformation twinning in fatigue crack tip plastic zone of Ti-6Al-4 V alloy with Widmanstatten microstructure. Mater. Charact. 132, 338–347. https://doi.org/10.1016/j.matchar.2017.08.029.

Margolin, H., Longo, R.B., 1979. Slip band spacings in alpha titanium. Scripta Metallurgica 13, 561–564. https://doi.org/10.1016/0036-9748(79)90108-X.

Medina Perilla, J.A., Gil Sevillano, J., 1995. Two-dimensional sections of the yield locus of a Ti⍰6%Al⍰4%V alloy with a strong transverse-type crystallographic α-texture. Materials Science and Engineering: A 201, 103–110. https://doi.org/10.1016/0921-5093(95)09780-5.

Miller, M.P., Pagan, D.C., Beaudoin, A.J., Nygren, K.E., Shadle, D.J., 2020. Understanding Micromechanical Material Behavior Using Synchrotron X-rays and In Situ Loading. Metall. Mater. Trans. A. https://doi.org/10.1007/s11661-020-05888-w.

Morris, P.R., 1970. Elastic constants of polycrystals. Int. J. Eng. Sci. 8, 49–61. https://doi.org/10.1016/0020-7225(70)90014-5.

Moulinec, H., Suquet, P., 1998. A numerical method for computing the overall response of nonlinear composites with complex microstructure. Comput. Methods Appl. Mech. Eng. 157, 69–94. https://doi.org/10.1016/S0045-7825(97)00218-1.

Nait-Ali, A., Hémery, S., Gueguen, M., 2021. How macrozone size and morphology influence yield in titanium alloys investigated using fast Fourier transform-based crystal plasticity simulations. Int. J. Solids. Struct. https://doi.org/10.1016/j.ijsolstr.2021.01.008.

Neeraj, T., Hou, D.H., Daehn, G.S., Mills, M.J., 2000. Phenomenological and microstructural analysis of room temperature creep in titanium alloys. Acta Mater. 48, 1225–1238. https://doi.org/10.1016/S1359-6454(99)00426-7.

Oliver, W.C., Pharr, G.M., 1992. An improved technique for determining hardness and elastic modulus using load and displacement sensing indentation experiments. J. Mater. Res. 7, 1564–1583. https://doi.org/10.1557/JMR.1992.1564.

Pagan, D.C., Peterson, K.M., Shade, P.A., Pilchak, A.L., Dye, D., 2023. Using the Ti–Al System to Understand Plasticity and Its Connection to Fracture and Fatigue in α Ti Alloys. Metall. Mater. Trans. A. https://doi.org/10.1007/s11661-023-07114-9.

Pagan, D.C., Shade, P.A., Barton, N.R., Park, J.S., Kenesei, P., Menasche, D.B., Bernier, J.V., 2017. Modeling slip system strength evolution in Ti-7Al informed by in-situ grain stress measurements. Acta Mater. 128, 406–417. https://doi.org/10.1016/j.actamat.2017.02.042.

Park, S., Jung, J., Cho, W., Jeong, B.S., Na, H., Kim, S.I., Lee, M.G., Han, H.N., 2021. Predictive dual-scale finite element simulation for hole expansion failure of ferrite-bainite steel. Int. J. Plast. 136, 102900 https://doi.org/10.1016/j.ijplas.2020.102900.

Prakash, D.G.L., Ding, R., Moat, R.J., Jones, I., Withers, P.J., Fonseca, J.Q.da, Preuss, M., 2010. Deformation twinning in Ti-6Al-4 V during low strain rate deformation to moderate strains at room temperature. Materials Science and Engineering: A 527, 5734–5744. https://doi.org/10.1016/j.msea.2010.05.039.

Risbet, M., Feaugas, X., Guillemer-Neel, C., Clavel, M., 2003. Use of atomic force microscopy to quantify slip irreversibility in a nickel-base superalloy. Scr. Mater. 49, 533–538. https://doi.org/10.1016/S1359-6462(03)00357-9.

Riyad, I.A., Feather, W.G., Vasilev, E., Lebensohn, R.A., McWilliams, B.A., Pilchak, A.L., Knezevic, M., 2021. Modeling the role of local crystallographic correlations in microstructures of Ti-6Al-4 V using a correlated structure visco-plastic self-consistent polycrystal plasticity formulation. Acta Mater. 203, 116502 https://doi.org/10.1016/j.actamat.2020.116502.

Roberts, W., Gong, J., Wilkinson, A.J., Tarleton, E., 2020. Tension–compression asymmetry of ⟨c+a⟩ slip in Ti–6Al. Scr. Mater. 178, 119–123. https://doi.org/10.1016/j.scriptamat.2019.11.002.

Ruiz de Sotto, M., Longère, P., Doquet, V., Papasidero, J., 2020. A constitutive model for a rate and temperature-dependent, plastically anisotropic titanium alloy. Int. J. Plast. 134, 102777 https://doi.org/10.1016/j.ijplas.2020.102777.

Semiatin, S.L., 2020. An Overview of the Thermomechanical Processing of α/β Titanium Alloys: Current Status and Future Research Opportunities. Metallurgical and Materials Transactions A 51, 2593–2625. https://doi.org/10.1007/s11661-020-05625-3.

Shen, J., Kotha, S., Noraas, R., Venkatesh, V., Ghosh, S., 2022. Developing parametrically upscaled constitutive and crack nucleation models for the α/β Ti64 alloy. Int. J. Plast. 151, 103182 https://doi.org/10.1016/j.ijplas.2021.103182.

Smith, B.D., Shih, D.S., McDowell, D.L., 2018a. Cyclic plasticity experiments and polycrystal plasticity modeling of three distinct Ti alloy microstructures. Int. J. Plast. 101, 1–23. https://doi.org/10.1016/j.ijplas.2013.10.004.

Smith, B.D., Shih, D.S., McDowell, D.L., 2018b. Cyclic plasticity experiments and polycrystal plasticity modeling of three distinct Ti alloy microstructures. Int. J. Plast. 101, 1–23. https://doi.org/10.1016/j.ijplas.2013.10.004.

Song, X., Zhang, S.Y., Dini, D., Korsunsky, A.M., 2008. Finite element modelling and diffraction measurement of elastic strains during tensile deformation of HCP polycrystals. In: Computational Materials Science, International Conference on Materials for Advanced Technologies 2007 (ICMAT 2007) Selected papers of Symposium O: Frontiers in Computational Materials Science, 44, pp. 131–137. https://doi.org/10.1016/j.commatsci.2008.01.043.

Stapleton, A.M., Raghunathan, S.L., Bantounas, I., Stone, H.J., Lindley, T.C., Dye, D., 2008. Evolution of lattice strain in Ti–6Al–4 V during tensile loading at room temperature. Acta Mater. 56, 6186–6196. https://doi.org/10.1016/j.actamat.2008.08.030.

Stinville, J.C., Charpagne, M.A., Cervellon, A., Hemery, S., Wang, F., Callahan, P.G., Valle, V., Pollock, T.M., 2022. On the origins of fatigue strength in crystalline metallic materials. Science (1979) 377, 1065–1071. https://doi.org/10.1126/science.abn0392.

Sun, Q., Guo, Q., Yao, X., Xiao, L., Greer, J.R., Sun, J., 2011. Size effects in strength and plasticity of single-crystalline titanium micropillars with prismatic slip orientation. Scr. Mater. 65, 473–476. https://doi.org/10.1016/j.scriptamat.2011.05.033.

Suri, S., Viswanathan, G.B., Neeraj, T., Hou, D.H., Mills, M.J., 1999. Room temperature deformation and mechanisms of slip transmission in oriented single-colony crystals of an α/β titanium alloy. Acta Mater. 47, 1019–1034. https://doi.org/10.1016/S1359-6454(98)00364-4.

Tari, V., Lebensohn, R.A., Pokharel, R., Turner, T.J., Shade, P.A., Bernier, J.V., Rollett, A.D., 2018. Validation of micro-mechanical FFT-based simulations using High Energy Diffraction Microscopy on Ti-7Al. Acta Mater. 154, 273–283. https://doi.org/10.1016/j.actamat.2018.05.036.

Truax, D.J., McMahon, C.J., 1974. Plastic behavior of titanium-aluminum alloys. Materials Science and Engineering 13, 125–139. https://doi.org/10.1016/0025-5416(74)90181-5.

Venkatraman, A., McDowell, D.L., Kalidindi, S.R., 2022. Bayesian analysis of parametric uncertainties and model form probabilities for two different crystal plasticity models of lamellar grains in α+β Titanium alloys. Int. J. Plast. 154, 103289 https://doi.org/10.1016/j.ijplas.2022.103289.

Venkatramani, G., Ghosh, S., Mills, M., 2007. A size-dependent crystal plasticity finite-element model for creep and load shedding in polycrystalline titanium alloys. Acta Mater. 55, 3971–3986. https://doi.org/10.1016/j.actamat.2007.03.017.

Waheed, S., Zheng, Z., Balint, D.S., Dunne, F.P.E., 2019. Microstructural effects on strain rate and dwell sensitivity in dual-phase titanium alloys. Acta Mater. 162, 136–148. https://doi.org/10.1016/j.actamat.2018.09.035.

Wang, L., Yang, Y., Eisenlohr, P., Bieler, T.R., Crimp, M.A., Mason, D.E., 2009. Twin Nucleation by Slip Transfer across Grain Boundaries in Commercial Purity Titanium. Metall. Mater. Trans. A 41, 421. https://doi.org/10.1007/s11661-009-0097-6.

Wei, S., Kim, J., Tasan, C.C., 2022. In-situ investigation of plasticity in a Ti-Al-V-Fe (α+β) alloy: Slip mechanisms, strain localization, and partitioning. Int. J. Plast. 148, 103131 https://doi.org/10.1016/j.ijplas.2021.103131.

Welsch, G., Boyer, R., Collings, E.W., 1993. Materials Properties Handbook: Titanium Alloys. ASM International.

Welsch, G., Bunk, W., 1982. Deformation modes of the α-phase of ti-6al-4v as a function of oxygen concentration and aging temperature. Metall. Mater. Trans. A 13, 889–899. https://doi.org/10.1007/BF02642403.

Williams, J.C., Baggerly, R.G., Paton, N.E., 2002. Deformation behavior of HCP Ti-Al alloy single crystals. Metall. Mat. Trans. A 33, 837–850. https://doi.org/10.1007/s11661-002-1016-2.

Williams, J.C., Thompson, A.W., Baggerly, R.G., 1974. Accurate description of slip character. Scripta Metallurgica 8, 625–630. https://doi.org/10.1016/0036-9748(74)90009-X.

Wu, Z., Curtin, W.A., 2016. Mechanism and energetics of ⟨c + a⟩ dislocation cross-slip in hcp metals. Proceedings of the National Academy of Sciences 113, 11137–11142. https://doi.org/10.1073/pnas.1603966113.

Xiong, Y., Grilli, N., Karamched, P.S., Li, B.S., Tarleton, E., Wilkinson, A.J., 2022. Cold dwell behaviour of Ti6Al alloy: Understanding load shedding using digital image correlation and dislocation based crystal plasticity simulations. J. Mater. Sci. Technol. 128, 254–272. https://doi.org/10.1016/j.jmst.2022.05.034.

Xu, X., Lunt, D., Thomas, R., Babu, R.P., Harte, A., Atkinson, M., da Fonseca, J.Q., Preuss, M., 2019. Identification of active slip mode in a hexagonal material by correlative scanning electron microscopy. Acta Mater. 175, 376–393. https://doi.org/10.1016/j.actamat.2019.06.024.

Zaefferer, S., 2003. A study of active deformation systems in titanium alloys: dependence on alloy composition and correlation with deformation texture. Materials Science and Engineering: A 344, 20–30. https://doi.org/10.1016/S0921-5093(02)00421-5.

Zhang, L., Jiang, B., Qiu, J., Cao, X., Lei, J., Yang, R., Du, K., 2023. The interface effect on crack nucleation under dwell fatigue loading in dual-phase Ti alloy. Int. J. Plast. 171, 103816 https://doi.org/10.1016/j.ijplas.2023.103816.

Zhang, P., Li, S.X., Zhang, Z.F., 2011. General relationship between strength and hardness. Materials Science and Engineering: A 529, 62–73. https://doi.org/10.1016/j.msea.2011.08.061.

Zhang, Z., Jun, T.S., Britton, T.B., Dunne, F.P.E., 2016a. Intrinsic anisotropy of strain rate sensitivity in single crystal alpha titanium. Acta Mater. 118, 317–330. https://doi.org/10.1016/j.actamat.2016.07.044.

Zhang, Z., Jun, T.S., Britton, T.B., Dunne, F.P.E., 2016b. Determination of Ti-6242 α and β slip properties using micro-pillar test and computational crystal plasticity. J. Mech. Phys. Solids. 95, 393–410. https://doi.org/10.1016/j.jmps.2016.06.007.

Zhang, Z., Jun, T.S., Britton, T.B., Dunne, F.P.E., 2016c. Determination of Ti-6242 α and β slip properties using micro-pillar test and computational crystal plasticity. J. Mech. Phys. Solids. 95, 393–410. https://doi.org/10.1016/j.jmps.2016.06.007.

Zheng, Z., Waheed, S., Balint, D.S., Dunne, F.P.E., 2018. Slip transfer across phase boundaries in dual phase titanium alloys and the effect on strain rate sensitivity. Int. J. Plast. 104, 23–38. https://doi.org/10.1016/j.ijplas.2018.01.011.